Harnessing transcription factor activity for programmable therapeutic gene regulation

Yingbo Jia[1,2,10], Chu-Yen Chen[1,10], Bo Zhu[1,2,3,10], Zhigui Wu[1,4], Yi-Chia Wu[1,6,7], Renqi Wang[1,2], Abdulmajeed I. Salamah[1], Sushmita Halder[1], Yen-Nien Liu[1,5], Yingjie Guo[8], Ying Chen[9], Luca Scimeca[1,2], Hang Yin[1,2], Tejas Sabu[1], Enoch B. Antwi[1,2], Yang Wang[1,2], Ming-Ru Wu[1,2,*]

[1]Department of Cancer Immunology and Virology, Dana-Farber Cancer Institute, Boston, MA 02215, USA.

[2]Department of Immunology, Harvard Medical School, Boston, MA 02115, USA.

[3]Department of Liver Surgery, Center of Hepato-Pancreato-Biliary Surgery, Institute of Precision Medicine, The First Affiliated Hospital, Sun Yat-sen University, Guangzhou 510080, China.

[4]Department of Pharmacy, Affiliated Hospital, Southwest Medical University, Luzhou 646000, China.

[5]Graduate Institute of Cancer Biology and Drug Discovery, College of Medical Science and Technology, Taipei Medical University, New Taipei City 235, Taiwan.

[6]Department of Surgery, College of Medicine, Kaohsiung Medical University, Kaohsiung, Taiwan.

[7]Division of Plastic and Reconstructive Surgery/Breast Oncology and Surgery, Department of Surgery, Kaohsiung Medical University Hospital, Kaohsiung, Taiwan.

[8]Arc Institute, Palo Alto, CA 94304, USA.

[9]Department of Ophthalmology and Visual Sciences, University of Michigan School of Medicine, Ann Arbor, MI 48105, USA.

[10]These authors contributed equally.

*Corresponding author. Email: ming-ru_wu@dfci.harvard.edu

Abstract

Transcription factors (TFs) regulate gene expression programs that define cellular identity, functional state, and disease progression. Despite their central role in biology and disease, only a small fraction of TFs are directly druggable, leaving most disease-associated TFs beyond pharmacological reach and limiting the development of TF-centric therapeutic strategies. Here we propose a generalizable regulatory framework that repurposes endogenous TF activity not as a therapeutic target, but as an intrinsic trigger for programmable gene control. Using high-throughput functional screening of synthetic enhancers, we decode TF activity with minimal regulatory elements that selectively respond to context-specific transcriptional programs. Applied to ovarian cancer, this framework enables the identification of cancer-selective synthetic enhancers that exploit aberrant TF activity to distinguish malignant cells from normal epithelial cells. By integrating these enhancers with protein interaction-based AND-gate circuits, multiple TF inputs are evaluated through Boolean logic, enabling enhanced tumor specificity and amplified transcriptional output. In murine ovarian cancer models, these circuits selectively drive combinatorial immune effector expression and trigger robust antitumor responses. Extending this framework beyond cancer, we identify activation-responsive synthetic enhancers in primary human T cells that leverage endogenous activation-induced TF programs. These enhancers achieve stronger inducibility with lower basal activity than conventional NFAT-based designs. Together, these results establish TF activity as a programmable regulatory signal that can be decoded, integrated, and deployed to enable precise and context-dependent therapeutic gene regulation.

Introduction

Transcription factors (TFs) regulate gene expression programs that define cellular identity, state transitions, and functional responses across diverse biological contexts (*1, 2*). In cancer, aberrant TF activity drives oncogenic programs that promote tumor initiation, progression, and immune evasion (*3*). In immune cells, coordinated and dynamic TF programs regulate activation-induced state transitions, lineage differentiation, and effector function (*4*). These observations underscore the central role of TF activity in defining disease- and context-specific cellular states.

Despite this central role, most TFs remain difficult to target therapeutically. Unlike enzymes or receptors, TFs typically lack catalytic activity and exert their functions through protein-DNA or protein-protein interactions that are poorly amenable to conventional small-molecule inhibition (*5*). As a result, TF-oriented therapeutic efforts have largely focused on indirect strategies, including modulation of upstream signaling pathways, downstream gene products, cofactors, or chromatin regulators (*6, 7*). More recently, emerging modalities such as targeted protein degradation have expanded the range of TFs that can be experimentally manipulated (*8*). However, these approaches remain applicable to only a limited subset of TFs with suitable molecular handles, leaving the majority of TF-driven regulatory programs therapeutically inaccessible. This limitation underscores the need for strategies that can engage the largely undruggable TF repertoire for therapeutic benefit, potentially unlocking new treatment avenues for diseases refractory to conventional approaches.

Here, we propose a complementary conceptual framework to bridge this gap by reinterpreting TFs not as pharmacological targets, but as endogenous regulatory signals for therapeutic gene control. Rather than attempting to perturb TF activity directly, this framework leverages endogenous TF activity as an intrinsic trigger to engage TF-driven regulatory states. To operationalize this concept, we introduce a generalizable strategy that functionally decodes TF activity through synthetic enhancer elements. Building on the principle that TFs regulate gene expression via enhancer binding, we developed the TREND (transcription factor-responsive enhancer discovery) platform as a functional screening approach to identify TF-responsive synthetic enhancers. These enhancers serve as programmable regulatory interfaces that convert endogenous TF activity into defined, context-dependent gene expression outputs, enabling TF activity to be functionally decoded, logically integrated, and deployed for precise therapeutic gene regulation. We apply this TF-activity-guided framework in both cancer and immune cell contexts,

establishing endogenous TF activity as a programmable, context-dependent regulatory signal that can be decoded and computed to control therapeutic gene expression in vivo.

Results

Functional decoding of TF activity reveals cancer-selective synthetic enhancers

To test whether endogenous TF activity can be directly and systematically decoded as a functional regulatory signal, we developed TREND, a lentiviral-based massively parallel reporter assay (MPRA) framework for high-throughput quantification of TF-responsive enhancer activity. Rather than inferring TF activity from transcript abundance or chromatin features such as motif accessibility or TF occupancy, TREND directly interrogates TF activity via the functional output of synthetic enhancers composed of defined TF binding sites. To enable broad coverage, we assembled a library of position probability matrices (PPMs) and position weight matrices (PWMs) for 1,068 human TFs from 14 public databases (*9*), including ENCODE, JASPAR, and CIS-BP (Fig. 1A). This collection spans 96.5% of TFs with known binding motifs and includes both lineage-determining factors and pan-cancer master regulators(*2*) (*10, 11*) (Fig. 1B), providing a generalizable framework for systematically decoding TF activity across cellular and disease contexts.

As TF binding motifs exhibit substantial diversity and context-dependent affinities (*12, 13*), we reasoned that individual motif variants could encode distinct binding strengths and transcriptional activation thresholds. For therapeutic gene regulation, such threshold differences are critical, as disease specificity often depends not on the mere presence of TF activity, but on whether TF activity exceeds a level that distinguishes pathological from normal cellular states. We therefore hypothesized that systematically incorporating multiple motif variants per TF would generate enhancers with a spectrum of activation sensitivities, increasing the likelihood of identifying regulatory elements capable of precise, context-specific gene control.

To capture this range of activation sensitivities, we extracted the ten most frequently occurring sequences generated by sampling each PPM or PWM, with the most frequent sequence representing the consensus and the remaining sequences treated as variants. Each synthetic enhancer design consisted of tandem repeats of a single TFBS sequence (consensus or variant) placed upstream of an adenoviral minimal promoter driving EGFP expression, with a unique DNA barcode that is co-transcribed with the reporter (*14, 15*). By pooling thousands of these constructs,

we generated a library of 57,715 synthetic enhancer-reporter elements for high-throughput screening.

To identify cancer-selective regulatory signals encoded by endogenous TF activity, we used the pooled synthetic enhancer library as a functional probe of transcriptional states. The library was packaged into lentiviruses and introduced into human immortalized ovarian surface epithelium cells (IOSE), human ovarian cancer OVCAR-8 (hereafter referred to as OV8) cells, and murine ovarian cancer (ID8) cells. IOSE cells were used as a surrogate for normal ovarian surface epithelium because they retain key epithelial features and transcriptional similarity to primary ovarian surface epithelial cells while permitting efficient lentiviral transduction and high-coverage screening (*16*).

In this framework, differential activity of individual synthetic enhancers serves as a direct functional readout of the underlying TF programs engaged in each cellular context. To enable high-throughput, parallel quantification of enhancer activity, barcode abundance was measured in both RNA and DNA by targeted next-generation sequencing (NGS), allowing normalization of transcriptional output to construct abundance. Each enhancer was associated with multiple unique barcodes, providing independent readouts of activity. This design helps account for variability arising from lentiviral integration site effects, intrinsic transcriptional noise, and potential enhancer-barcode mismatches, thereby reducing the influence of outliers. For each enhancer, RNA/DNA ratios were calculated at the individual-barcode level, and the median value across all associated barcodes was used as the final measure of enhancer activity within each biological replicate. By leveraging multiple independent barcode measurements per enhancer, this approach provides a robust and quantitative measure of enhancer-driven expression across both normal and cancer contexts. Mean values across biological replicates were then used to represent the overall activity for each construct.

Based on these barcode-derived activity scores, each synthetic enhancer can be classified as preferentially active in normal cells or cancer cells, broadly active in both, or inactive in both contexts. Sequencing data were processed through a standardized pipeline including sample demultiplexing, unique molecular identifier (UMI) collapsing to correct for PCR amplification bias, and alignment to the reference library to map barcodes to their corresponding enhancer constructs. Transcript-per-million (TPM) normalization was applied to account for differences in sequencing depth across samples. Quality filtering based on DNA abundance and barcode

representation was used to exclude low-confidence elements, supporting robust and reproducible quantification across the entire library (Fig. 1C). Consistent with the broad and diverse library design, enhancer activity in IOSE and OV8 cells spanned a wide dynamic range, with most elements exhibiting comparable output across contexts and a distinct subset displaying markedly elevated OV8/IOSE activity ratios, identifying candidate cancer-selective synthetic enhancers (Fig. 1D). Activity profiles were highly reproducible across biological replicates, with strong inter-experimental correlations (fig. S1), supporting the reliability of these functional measurements.

Because transcription factor expression is often used as a proxy for regulatory activity, we next asked whether TF mRNA abundance alone could predict the performance of synthetic enhancers identified by TREND. To address this question, we compared TREND-measured enhancer activity with RNA-seq-based TF differential expression between OV8 and IOSE cells. No meaningful correlation was observed (Fig. 1E): the most cancer-selective enhancers were not associated with TFs showing the largest expression differences (Fig. 1F), and conversely, enhancers linked to highly differentially expressed TFs did not exhibit strong cancer specificity (Fig. 1G). Together, these results demonstrate that TF expression alone is a poor predictor of functional, context-specific enhancer activity, underscoring the importance of direct functional screening approaches for uncovering regulatory elements capable of highly context-specific gene control.

Among the top cancer-specific enhancers, specificity did not correlate with motif rank within the PPM or PWM. For a given motif matrix, the most cancer-selective enhancer could derive from either the consensus sequence or lower-probability variants (fig. S2A), indicating that motif probability alone is not predictive of enhancer specificity. Instead, motif variants can encode distinct binding affinities that impose different activation thresholds. Sampling a large number of such variants enables identification of enhancers whose activation thresholds fall between TF activity levels in normal and cancer cells, remaining inactive in normal cells while becoming robustly activated in tumors. This threshold positioning is consistent with the sharp on/off behavior and high specificity observed for the selected enhancers. Accordingly, systematic incorporation of motif variants expands the accessible regulatory space and increases the likelihood of identifying synthetic enhancers with highly context-specific gene regulation.

Consistent with the broad dynamic range observed in the screen, TREND revealed multiple classes of synthetic enhancers, including those selectively active in human cancer cells (high

OV8/IOSE), mouse cancer cells (high ID8/IOSE), and shared cancer-selective elements active in both human and mouse cancer cells (high OV8/IOSE and ID8/IOSE), as well as enhancers preferentially active in immortalized human epithelial cells (high IOSE/OV8, high IOSE/ID8, or both). These results highlight the versatility of this approach in identifying diverse, context-dependent enhancer activities across species and cellular states (fig. S2B).

Collectively, these results demonstrate that endogenous TF activity can be directly and systematically decoded through synthetic regulatory elements, providing a functional foundation for context-specific gene regulation.

Cancer-selective synthetic enhancers report cognate TF activity

To test whether TREND-identified enhancers function as robust and cancer-selective regulatory elements, we individually cloned top candidates and evaluated their activity in ovarian cancer (OV8) and immortalized epithelial (IOSE) cells. Quantitative reporter assays were performed by placing each enhancer upstream of an adenoviral minimal promoter driving EGFP, followed by lentiviral delivery into OV8 and IOSE cells. Several motif variants from the MYC and E2F families consistently showed strong activity in OV8 cells while remaining largely inactive in IOSE (Fig. 2A). Given their pronounced activity and cancer specificity, together with their sequence diversity, MYC_v4 and E2F_v2 were selected as representative synthetic enhancers for further analysis. When introduced into OV8 and IOSE cells, both enhancers produced strong and uniform fluorescence in OV8, whereas IOSE cells displayed only background-level signal (Fig. 2B). Together, these results suggest that TREND can nominate synthetic enhancers with robust and cancer-selective activity.

We next asked whether these enhancers act as quantitative, TF-specific readouts of endogenous TF activity, rather than as non-specific reporters of cancer state. To test this, we focused on two validated candidates, MYC_v4 and E2F_v2, and examined whether enhancer activity scaled with cognate TF abundance. Each enhancer was co-transduced with an inducible TF overexpression cassette, allowing TF levels to be tuned by varying the inducer dose. Reporter assays in IOSE cells revealed clear dose-response relationships: increasing MYC or E2F4 levels selectively enhanced activity from the matched enhancer, whereas activity from the unmatched enhancer remained largely unchanged (Fig. 2, C and D, and fig. S3). Although this analysis focused on two representative enhancers rather than the entire library, the observed dose-dependent

increase in activity with cognate TF abundance is consistent with the TF-centric design of the enhancer library. Together, these results support the expectation that TREND-nominated elements can reflect the activity of their corresponding TFs.

In our previous study, we demonstrated that synthetic enhancers can achieve higher specificity than native cancer-specific promoters (*17*). To further evaluate whether TREND-derived synthetic enhancers provide improved functional performance over those earlier manually designed constructs, we compared the top-performing TREND candidates with our prior design. Reporter assay showed that TREND-derived synthetic enhancers drove stronger activity in cancer cells while maintaining markedly improved specificity (Fig. 2, E and F). These results demonstrate the advantage of systematic, high-throughput functional screening over rational design in identifying synthetic enhancers with superior activity and specificity.

Combinatorial TF sensing enhances cancer-restricted gene expression

Although individual TREND-derived enhancers exhibited high cancer selectivity, low-level background activity could still be detected in certain normal cells. Because endogenous TF activity is leveraged here as a functional regulatory input rather than a pharmacological target, it can be logically integrated to further enhance specificity. Transcriptional output can therefore be gated by defined combinations of multiple, independent TF activities, restricting gene expression to cells in which all required inputs are satisfied simultaneously. This AND-gate logic confines activity to disease-specific transcriptional states that are unlikely to arise in healthy tissues.

To implement this logic, each TREND-derived enhancer was used to drive expression of one half of a split transcription factor: a GAL4 DNA-binding domain (GAL4BD) fused to a leucine-zipper domain, or a VP16 activation domain (VP16AD) fused to its complementary zipper partner. Only when both enhancers are active are the two components produced simultaneously, allowing the zipper domains to associate and reconstitute a functional GAL4BD-VP16AD transcriptional activator (GAD).

To identify effective leucine-zipper pairs for reconstitution, we assembled a library of 55 previously characterized heterodimeric coiled-coil domains, including the canonical SYNZIP set and additional validated interaction pairs from published studies (*18, 19*) (Fig. 3A). All possible 55 × 55 combinations were tested in a pooled format, with each candidate fused to either the GAL4BD (GAL4BD-zipper) or the VP16AD (zipper-VP16AD). When two compatible zippers

interact, the GAL4BD-zipper and zipper-VP16AD components associate to reconstitute a functional GAD, which activates a GAL4 promoter driving further expression of the same GAL4BD-zipper and zipper-VP16AD pair. This positive-feedback loop amplifies transcripts of interacting pairs, allowing their relative abundance to serve as a quantitative readout of interaction strength. Because HEK293T cells do not express GAD endogenously, we incorporated a Tet-ON inducible system to transiently provide baseline GAD activity across all cells (*20*). This initial induction triggers low-level transcription of each candidate pair; if the paired zippers interact, they sustain and amplify their own expression through the feedback loop, whereas non-interacting pairs quickly decay after the initial induction.

To ensure that each cell expressed only one candidate pair, viral delivery was performed at low multiplicity of infection. RNA sequencing of zipper transcripts revealed a range of interaction strengths across all tested pairs (Fig. 3B). To capture this diversity, we selected several representative pairs spanning weak to strong interactions, as highlighted with circles in Fig. 3B, for subsequent construction of AND gate circuits. Flow cytometry analysis showed that the SYNZIP5-SYNZIP12 combination produced the strongest reporter activation among the pairs examined (Fig. 3C).

To confirm that our split-transcription factor design exhibits AND-gate behavior, we examined whether partial circuit configurations could activate the reporter. Cells were transiently transfected with three expression cassettes: two constitutively expressed input modules, driven by the CMV promoter, encoding GAL4BD-SYNZIP2 and SYNZIP1-VP16AD, and a third output module in which the reconstituted GAD drives mKate expression. We evaluated three input combinations: [1,0] (only module 1 present), [0,1] (only module 2 present), and [1,1] (both modules present). Reporter expression was detected exclusively in the [1,1] condition, while [1,0] and [0,1] configurations showed no detectable signal (fig. S4A). These prototyping experiments, performed in HEK293T cells to enable rapid and efficient testing, show that the split-transcription factor design enforces AND-gate behavior, restricting gene activation to cells in which both inputs are present.

We next tested whether the same design remains functional when delivered by lentivirus for stable genomic integration, as intended for application in tumor models. The circuit components were introduced into both human OV8 and murine BPPNM ovarian cancer cells using lentiviral transduction. Reporter assays revealed robust activation in both lines (fig. S4B), demonstrating

that the AND-gate circuit performs reliably in integrated formats across species. Furthermore, the output strength can be tuned by selecting different SYNZIP interaction pairs, highlighting the modular and adjustable nature of the system.

After selecting representative SYNZIP pairs, we next sought to determine how best to incorporate them into split TFs. Because the optimal positioning of SYNZIP domains within the split TF was unclear, we systematically evaluated three fusion configurations. Reporter assays revealed that transcriptional activation occurred only when the SYNZIP was fused to the C terminus of GAL4BD and the N terminus of VP16AD (fig. S4, C and D). Alternative orientations failed to restore activity, emphasizing the importance of domain arrangement for complex reconstitution. Incorporating a nuclear localization signal (NLS) into VP16AD further enhanced reporter expression, indicating that efficient nuclear targeting improves transcriptional activation (fig. S4E).

To evaluate whether TREND-derived synthetic enhancers can serve as inputs for AND gate computation, we selected six validated human ovarian cancer-specific enhancers (MYC_v4, E2F7_v3, MYC_v2, E2F_v2, FOS, and BACH1) and paired them systematically in all possible two-input combinations (6 × 6 matrix). The schematic of the modular AND-gate circuit is shown in Fig. 3D: one synthetic enhancer drives the expression of GAL4BD fused to SYNZIP5 (module 1), and the other drives VP16AD fused to its complementary partner, SYNZIP12 (module 2). Transcriptional activation occurs only when both enhancers are active, allowing the two fusion proteins to assemble into a functional GAD that induces the expression of the downstream mKate reporter. Screening across the enhancer pair matrix identified several combinations that exhibited strong and cancer-restricted activity in OV8 cells while remaining largely inactive in IOSE cells (Fig. 3, E and F, and fig. S5A). These results demonstrate that specific TREND-derived enhancer pairs can cooperate through the AND-gate circuit to achieve highly cancer-selective transcriptional activation. Compared with our earlier AND-gate design reported previously (*17*), the current system achieved substantially higher specificity (fig. S5B). When compared with single-enhancer configurations, the AND-gate also amplified transcriptional output, producing stronger reporter expression and sharper cancer-to-normal discrimination (fig. S5, C and D).

Because single synthetic enhancers can exhibit low-level background activity in certain normal cells, we further tested whether the AND-gate configuration could improve targeting precision. From prior study, MYC- and E2F-based synthetic enhancers show minimal basal

activity across multiple primary human cell types (e.g., dermal fibroblasts, ovarian fibroblasts, and ovarian microvascular endothelial cells), non-tumorigenic breast cell lines (e.g., MCF-10A and MCF-12A), and induced pluripotent stem cells (*17*). However, MYC-based enhancers displayed modest activity in a non-tumorigenic colonic epithelial cell line (CCD-841 CoN), and E2F-based enhancers also exhibited modest basal activity in primary human T cells. To assess whether AND-gate circuits reduce this background activity, we compared the activity of single enhancers and AND-gate circuits in CCD-841 CoN cells and primary T cells. While single-enhancer constructs showed notable activity, the AND-gate circuits exhibited a pronounced reduction in background activity (fig. S5, E and F). Thus, AND-gate integration functions as a computational filter on TF-driven transcription, increasing specificity while maintaining or enhancing transcriptional output. Collectively, these results demonstrate that TREND-derived synthetic enhancers can be logically composed to enable precise and high-fidelity transcriptional control.

Tumor-restricted AND-gate circuits drive conditional combinatorial immunotherapy in vivo

Having shown that TREND-derived synthetic enhancers can be logically composed to integrate multiple TF activities, we next asked whether such transcriptional computation could be translated into tumor-restricted therapeutic programs in vivo. Specifically, we tested whether these circuits could conditionally drive the in situ production of multiple immunomodulatory payloads within tumors.

To translate this framework into murine in vivo models, we applied the pipeline to the ID8 ovarian cancer cell line, using IOSE cells as a reference to identify candidate mouse-specific synthetic enhancers (fig. S6, A and B). ID8 is a well-established and widely used murine model of ovarian cancer, providing an accessible starting point for subsequent in vivo evaluation. As the genetically defined BPPNM model later became available (*21*), we prioritized it for downstream studies because it more closely reflects the genomic alterations commonly observed in human ovarian cancer. To achieve broad coverage across model systems, we combined both human- and mouse-validated synthetic enhancers and evaluated their activity in BPPNM cells to identify cancer-selective candidates. We further evaluated these enhancers in two additional murine ovarian cancer models, KPCA and PPNM, which, together with BPPNM, constitute a panel of genetically engineered models encompassing the most frequent driver mutations observed in human ovarian

cancer. From these analyses, several enhancer variants derived from the PPMs of ZBTB33 and MYC families showed the strongest and most consistent cancer-specific activity in BPPNM cells (fig. S6, C to E). To support robust logical integration, we selected two sequence-divergent enhancer variants, ZBTB33_v2 and MYC_v2, as AND-gate inputs for proof-of-concept testing in the BPPNM ovarian cancer model.

We first assessed targeting precision and off-targeting expression in vivo, as these parameters are critical for clinical translation. BPPNM tumor-bearing mice and tumor-free wild-type C57BL/6 control mice were intraperitoneally administered lentiviral vectors encoding luciferase under the control of the synthetic enhancers (Fig. 4A). Bioluminescence imaging revealed that luminescent signals were confined to tumor-bearing mice, with only background-level activity observed in healthy controls (Fig. 4, B and C). To exclude limited viral delivery as a potential explanation for the absence of signal in normal tissues, we included a CMV promoter control, which drove widespread expression in the spleen, peritoneal wall, and tumor (Fig. 4, D and E). In contrast, the AND-gate circuit restricted luciferase activity to tumor sites. Together, these findings demonstrate that the AND-gate gene circuits achieve robust, tumor-selective activation with minimal off-target expression, highlighting their potential as an effective platform for in vivo therapeutic applications.

With tumor-restricted expression demonstrated in vivo, we next deployed this logic computation to orchestrate multiple immunomodulatory functions within tumors. We retained the same circuit architecture illustrated in Fig. 3C, but reconfigured the output module to drive expression of therapeutic effectors rather than fluorescent reporters (fig. S7). Effective antitumor immunity is often constrained by multiple, concurrent barriers within the tumor microenvironment, including limited tumor antigen engagement, insufficient T-cell co-stimulation, and suppressive signaling that dampens effector responses (*22*). To address these challenges in a coordinated manner, we assembled a panel of immunomodulators designed to target complementary aspects of tumor immunity. A surface T-cell engager (STE), consisting of a tumor-displayed anti-CD3ε single-chain variable fragment (scFv), was incorporated to promote direct T cell-tumor cell engagement, while CD80 provided co-stimulatory signaling to enhance T-cell activation (*23-25*). IL-12 was incorporated to support T_H1 polarization and effector differentiation, and Fms-related receptor tyrosine kinase 3 ligand (FLT3LG) was selected to expand dendritic cells (DCs) and promote antigen presentation (*26, 27*). To facilitate immune cell recruitment to the tumor milieu, we included CCL21(*28*). In addition, the N-terminal fragment of Gasdermin D (GSDMD-N) was

used to induce immunogenic tumor cell death, and an anti-PD-1 scFv was designed to locally alleviate checkpoint-mediated inhibition and restore T-cell function (*29, 30*).

We evaluated multiple combinations of these payloads in the BPPNM ovarian cancer model, including SCIP (STE, CCL21, IL-12, anti-PD-1 scFv), S8FP (STE, CD80, FLT3LG, anti-PD-1 scFv), S8IP (STE, CD80, IL-12, anti-PD-1 scFv), SFIP (STE, FLT3LG, IL-12, anti-PD-1 scFv), S8GP (STE, CD80, GSDMD-N, anti-PD-1 scFv), and SFGP (STE, FLT3LG, GSDMD-N, anti-PD-1 scFv), to identify therapeutic modules capable of reducing tumor burden and reprogramming the tumor microenvironment. Mice receiving the S8IP combination exhibited prolonged survival compared with controls (Fig. 4F). Bioluminescence imaging confirmed reduced tumor burden, and quantification analysis identified the S8IP module comprising STE, CD80, IL-12, and anti-PD-1 scFv as producing the strongest therapeutic effect (Fig. 4, G and H). Increasing the dosage of this circuit treatment further enhanced tumor control and extended survival, consistent with a dose-dependent therapeutic response (Fig. 4, I and J). Together, these results demonstrate that tumor-specific synthetic circuits coordinating multiple immunomodulators can elicit robust therapeutic benefit in vivo.

With potent, tumor-restricted activity established in vivo, we next examined whether tumor-restricted execution of this combinatorial program reshapes the immune microenvironment. Flow cytometry analysis of peritoneal immune cells revealed broad remodeling of immune composition following S8IP treatment (Fig. 4K). Specifically, the proportions of total $CD4^+$ and $CD8^+$ T cells, central and effector memory T cell subsets, Granzyme B^+ cytotoxic $CD8^+$ T cells, and IFN-γ^+ T_H1 cells were markedly increased, consistent with enhanced adaptive immune activation. In parallel, increased frequencies of total macrophages, M1-like macrophages, and DCs suggest a shift in the myeloid compartment toward an immunostimulatory phenotype (*31-33*). Together, these findings demonstrate that S8IP treatment not only reduces tumor burden but also reshapes the tumor microenvironment toward a coordinated pro-inflammatory state that supports durable antitumor immunity.

To further characterize these responses, we analyzed additional immune subsets. Both $CD4^+$ and $CD8^+$ T cells showed an increased proportion of PD-1^+ cells, a feature associated with recent activation as well as checkpoint regulation (fig. S8A). In the context of expanded effector populations and enhanced inflammatory responses, this increase is more consistent with active engagement rather than terminal exhaustion. In contrast, other immune populations, including

natural killer (NK) cells, natural killer T (NKT) cells, cytotoxic NK cells, regulatory T (Treg) cells, Ly6C^{high} monocytes, neutrophils, conventional type 1 dendritic cells (cDC1s) and cDC2s remained largely unchanged (fig. S8, B and C). Together, these findings suggest that the therapeutic circuits act primarily through enhancing the T cell-mediated immunity, with potential contributions from myeloid effector activity, consistent with the design of the S8IP module to potentiate T cell-driven anti-tumor immune responses.

Collectively, these results demonstrate that TREND-derived synthetic enhancers, when integrated into AND-gate gene circuits, compute transcriptional outputs from endogenous TF activity to drive localized execution of multiple immune effector functions. By coupling transcriptional computation with combinatorial immunotherapy, this framework supports potent, spatially confined antitumor responses while minimizing off-target immune activation.

Activation-responsive synthetic enhancers for T cell activation-specific gene control

To determine whether TF-activity-based regulatory control extended beyond tumor-associated transcriptional states, we applied the TREND framework to immune cell engineering. Because T cell activation involves the coordinated induction of multiple TFs downstream of antigen receptor signaling, endogenous TF activity represents a rich and actionable signal for coupling therapeutic gene expression to T cell activation. Although activation-responsive transgene control has been explored in adoptive cell therapies, commonly used multimerized NFAT-based synthetic enhancers often exhibit basal activity in resting T cells, resulting in unwanted background expression that can trigger premature effector release or systemic immune activation (*34, 35*). These limitations underscore the need for regulatory elements that combine robust activation-dependent induction with minimal off-state leakage.

To address this need, we used the TREND platform to identify synthetic enhancers that respond selectively and stringently to T cell activation. Because primary human T cells vary substantially across donors in proliferation, transduction efficiency, and activation sensitivity (*36, 37*), we sought to discover robust enhancer elements that function reproducibly across multiple human donors rather than donor-specific ones. Primary human T cells from two independent donors were first activated and transduced with the pooled TREND lentiviral library. After returning to a resting state, cells were stimulated, and enhancer-driven reporter activity was quantified by NGS of barcode-linked transcripts (Fig. 5A). This workflow enabled direct

comparison of enhancer activity between resting and activated states. From this screen, we identified a set of candidate activation-responsive enhancers, including NFKB1_v1, FOSL2, BCL, REL, RELA, FOSL1_v1, NFKB2, FOSL1_v2, NFKB1_v2, AP1_v3, AP1_v1, NFAT_v1, AP1_v2, and NFAT_v2, which showed strong induction upon T cell activation while remaining relatively silent in the resting state.

We next validated these candidates individually in primary human T cells from three independent donors. Across donors, most enhancers exhibited markedly higher activity in the activated state than in the resting state (Fig. 5, B and C, and fig. S9, A to F). Notably, several candidates, including NFKB1_v1, BCL, REL, RELA, and NFKB1_v2, also showed substantially elevated basal EGFP expression in resting T cells, indicating incomplete off-state silencing (Fig. 5D, and fig. S9, C and F). Among all elements tested, FOSL1_v1 consistently demonstrated the highest activation specificity, driving robust reporter expression upon stimulation while maintaining near-background activity in resting cells across all donors.

To confirm that these results reflected enhancer-intrinsic regulatory performance rather than differences in T cell activation, we measured expression of CD25, a canonical activation marker, and observed comparable induction across all conditions (fig. S9G). This supports the interpretation that variation in enhancer-driven reporter output arose from differences in regulatory performance rather than unequal activation efficiency. Consistent with this interpretation, direct comparison with a conventional NFAT-motif-based enhancer showed that FOSL1_v1 exhibited markedly lower basal expression in resting T cells while driving stronger reporter induction upon stimulation (Fig. 5, E to J, and fig. S10). T cells transduced with either construct displayed similar CD25 expression, further supporting equivalent activation states (Fig. 5H). Collectively, these results demonstrate that FOSL1_v1 functions as a tighter and more precise transcriptional switch than existing NFAT-based designs, potentially enabling more stringent activation-dependent control of therapeutic payload expression in engineered T cells. Taken together, these findings demonstrated that TF-activity-based regulatory control extends beyond tumor contexts to enable activation-dependent gene expression in primary human T cells.

Discussion

TFs govern cellular identity, state transitions, and disease progression, yet their therapeutic exploitation has long been constrained by limited druggability and the difficulty of selectively

manipulating TF activity in vivo (*5*). In this study, we propose a conceptual shift in therapeutic gene regulation by treating endogenous TF activity not as a pharmacological target, but as an intrinsic regulatory signal that can be decoded, integrated, and deployed to control gene expression, thereby enabling therapeutic engagement of the broad and largely undruggable TF repertoire.

A defining feature of this framework is the use of synthetic enhancers as minimal and interpretable sensors of endogenous TF activity. Unlike endogenous regulatory elements shaped by complex and entangled inputs (*38*), synthetic enhancers derived from defined TF binding motifs provide a more direct functional interface between TF activity and transcriptional output. Through high-throughput functional screening, the TREND framework enables identification of TF-responsive enhancers without reliance on TF expression levels, chromatin annotations, or prior cis-regulatory knowledge. Importantly, the activity of top-performing enhancers showed no relationship to TF mRNA abundance, demonstrating that differential TF expression alone is insufficient to identify regulatory elements with strong context specificity. In other words, it is not obvious a priori which TFs, based solely on tumor-versus-normal expression differences, can serve as effective transcriptional triggers for disease-restricted gene regulation. These results highlight the limitations of rational TF selection strategies that rely on expression-based analyses rather than functional readouts of TF activity. In addition, enhancer performance did not correlate with motif rank within a given position weight matrix. Highly context-specific enhancers frequently arose from lower-probability motif variants rather than the consensus sequence, underscoring that motif probability alone does not predict functional specificity. This observation motivates the construction of large and diverse synthetic enhancer libraries that systematically sample motif variants, as the most functionally effective regulatory elements cannot be reliably inferred from consensus TF-binding sites alone. Together, these findings demonstrate that functional screening is a critical requirement for decoding context-specific TF activity and identifying effective synthetic enhancers.

Importantly, the advance of this work lies not only in generating improved synthetic enhancers, but in operationalizing a TF-activity-guided framework for gene regulation. Within this framework, synthetic enhancers function as minimal sensors of endogenous transcriptional programs identified through functional screening, rather than as DNA sequences chosen in advance based on TF identity or motif consensus. This framework treats TF activity as an explicit regulatory

signal that can be functionally interpreted and deployed to control gene expression across diverse cellular settings in a context-dependent manner.

Building on this foundation, our results further demonstrate that endogenous TF signals can be logically composed to compute higher-order regulatory decisions that depend on specific combinations of TF activity. By implementing protein interaction-based AND-gate circuits, multiple TF-responsive enhancers are integrated to restrict gene expression to cells in which distinct TF activities are simultaneously engaged. This architecture establishes that TF activity is a computable signal in living cells, such that transcriptional output reflects the result of logical operations performed on endogenous regulatory inputs rather than the activation of a single marker.

Applying this TF-activity-guided logic in vivo, AND-gate circuits sense and integrate tumor-associated transcriptional inputs to drive spatially confined therapeutic programs. In this framework, therapeutic execution is determined by endogenous regulatory inputs, directly coupling disease-associated TF activity to in vivo intervention.

Building on this framework, we evaluated its in vivo performance in murine ovarian cancer models by implementing synthetic enhancer-driven AND-gate circuits encoding immune effector modules. Treatment was associated with reduced tumor burden, prolonged survival, and induction of a pro-inflammatory tumor microenvironment. Among the tested configurations, the S8IP module, comprising STE, CD80, IL-12, and anti-PD-1 scFv, produced the strongest therapeutic response in a dose-dependent manner.

A critical test of any proposed regulatory framework is its generalizability beyond a single biological context. By extending this framework to primary human T cells, we demonstrate that TF-activity-guided enhancer discovery enables activation-dependent gene control with tighter off-state silencing and stronger inducibility than conventional NFAT-based designs. Together, these results demonstrate that the regulatory logic described here extends beyond tumor-associated transcriptional activity and can be applied to dynamic immune activation, supporting broader adaptation of TF-activity-guided regulation across cellular contexts.

Several limitations should be considered. The current implementation leverages TF activity through minimal regulatory logic to achieve robust, interpretable, and context-restricted control of therapeutic gene expression. While this architecture is sufficient to support tumor-selective therapeutic execution and immune modulation in the models tested, future extensions could explore whether incorporating additional regulatory dimensions, such as integrating more

enhancer inputs at the circuit level, enabling combinatorial TF sensing of multiple TF activities, or introducing temporal control of gene expression, further improves selectivity or robustness in specific disease contexts. In addition, integrating TF-activity-guided enhancer discovery with quantitative modeling or data-driven predictive frameworks may help prioritize enhancer-circuit configurations that best match the transcriptional features of a given disease context, thereby reducing empirical search space while preserving functional specificity.

In summary, this study demonstrates that endogenous TF activity can be functionally decoded, logically integrated, and deployed to control therapeutic gene expression. By shifting the focus from pharmacological TF targeting to transcriptional computation, this framework provides a principled basis for precise, context-dependent gene regulation, with demonstrated relevance to cancer treatment and immune engineering and the potential for broader applicability beyond these settings.

Reference

1. F. Spitz, E. E. Furlong, Transcription factors: from enhancer binding to developmental control. *Nat Rev Genet* **13**, 613-626 (2012).
2. S. A. Lambert *et al.*, The Human Transcription Factors. *Cell* **172**, 650-665 (2018).
3. M. Tufail, C. H. Jiang, N. Li, Immune evasion in cancer: mechanisms and cutting-edge therapeutic approaches. *Signal Transduct Target Ther* **10**, 227 (2025).
4. J. T. Chang, E. J. Wherry, A. W. Goldrath, Molecular regulation of effector and memory T cell differentiation. *Nat Immunol* **15**, 1104-1115 (2014).
5. M. J. Henley, A. N. Koehler, Advances in targeting 'undruggable' transcription factors with small molecules. *Nat Rev Drug Discov* **20**, 669-688 (2021).
6. X. Yang *et al.*, Targeting epigenetic and post-translational modifications of NRF2: key regulatory factors in disease treatment. *Cell Death Discov* **11**, 189 (2025).
7. J. H. Bushweller, Targeting transcription factors in cancer - from undruggable to reality. *Nat Rev Cancer* **19**, 611-624 (2019).
8. D. A. Nalawansha, C. M. Crews, PROTACs: An Emerging Therapeutic Modality in Precision Medicine. *Cell Chem Biol* **27**, 998-1014 (2020).
9. P. Shannon, M. Richards. (Bioconductor, 2025).
10. J. Reddy *et al.*, Predicting master transcription factors from pan-cancer expression data. *Sci Adv* **7**, eabf6123 (2021).
11. A. C. D'Alessio *et al.*, A Systematic Approach to Identify Candidate Transcription Factors that Control Cell Identity. *Stem Cell Reports* **5**, 763-775 (2015).
12. J. F. Kribelbauer-Swietek *et al.*, Context transcription factors establish cooperative environments and mediate enhancer communication. *Nat Genet* **56**, 2199-2212 (2024).
13. D. J. Burgess, Regulatory elements: Putting enhancers into context. *Nat Rev Genet* **17**, 377 (2016).
14. J. K. Cheng, H. S. Alper, Transcriptomics-Guided Design of Synthetic Promoters for a Mammalian System. *ACS Synth Biol* **5**, 1455-1465 (2016).
15. M. R. Wu *et al.*, A high-throughput screening and computation platform for identifying synthetic promoters with enhanced cell-state specificity (SPECS). *Nat Commun* **10**, 2880 (2019).
16. H. Y. Shin *et al.*, Establishment of five immortalized human ovarian surface epithelial cell lines via SV40 T antigen or HPV E6/E7 expression. *PLoS One* **13**, e0205297 (2018).
17. L. Nissim *et al.*, Synthetic RNA-Based Immunomodulatory Gene Circuits for Cancer Immunotherapy. *Cell* **171**, 1138-1150 e1115 (2017).
18. I. Sadowski, J. Ma, S. Triezenberg, M. Ptashne, GAL4-VP16 is an unusually potent transcriptional activator. *Nature* **335**, 563-564 (1988).
19. A. W. Reinke, R. A. Grant, A. E. Keating, A synthetic coiled-coil interactome provides heterospecific modules for molecular engineering. *J Am Chem Soc* **132**, 6025-6031 (2010).
20. A. T. Das, L. Tenenbaum, B. Berkhout, Tet-On Systems For Doxycycline-inducible Gene Expression. *Curr Gene Ther* **16**, 156-167 (2016).
21. S. Iyer *et al.*, Genetically Defined Syngeneic Mouse Models of Ovarian Cancer as Tools for the Discovery of Combination Immunotherapy. *Cancer Discov* **11**, 384-407 (2021).
22. K. G. Anderson, I. M. Stromnes, P. D. Greenberg, Obstacles Posed by the Tumor Microenvironment to T cell Activity: A Case for Synergistic Therapies. *Cancer Cell* **31**, 311-325 (2017).

23. H. Raskov, A. Orhan, J. P. Christensen, I. Gogenur, Cytotoxic CD8(+) T cells in cancer and cancer immunotherapy. *Br J Cancer* **124**, 359-367 (2021).
24. S. J. Zhou, M. G. Liu, F. Ren, X. J. Meng, J. M. Yu, The landscape of bispecific T cell engager in cancer treatment. *BIOMARKER RESEARCH* **9**, (2021).
25. K. W. Liao *et al.*, Stable expression of chimeric anti-CD3 receptors on mammalian cells for stimulation of antitumor immunity. *Cancer Gene Ther* **10**, 779-790 (2003).
26. M. D. Powell, K. A. Read, B. K. Sreekumar, D. M. Jones, K. J. Oestreich, IL-12 signaling drives the differentiation and function of a T(H)1-derived T(FH1)-like cell population. *Sci Rep* **9**, 13991 (2019).
27. H. Salmon *et al.*, Expansion and Activation of CD103+ Dendritic Cell Progenitors at the Tumor Site Enhances Tumor Responses to Therapeutic PD-L1 and BRAF Inhibition. *IMMUNITY* **44**, 924-938 (2016).
28. Y. Lin, S. Sharma, M. S. John, CCL21 Cancer Immunotherapy. *Cancers (Basel)* **6**, 1098-1110 (2014).
29. R. Chen, J. Zou, J. Liu, R. Kang, D. Tang, DAMPs in the immunogenicity of cell death. *Mol Cell* **85**, 3874-3889 (2025).
30. S. A. Patel, A. J. Minn, Combination Cancer Therapy with Immune Checkpoint Blockade: Mechanisms and Strategies. *IMMUNITY* **48**, 417-433 (2018).
31. J. Han *et al.*, Long-acting IL-2 release from pressure-fused biomineral tablets promotes antitumor immune response. *Nat Cancer* **6**, 1384-1399 (2025).
32. E. D. Kramer, S. I. Abrams, Granulocytic Myeloid-Derived Suppressor Cells as Negative Regulators of Anticancer Immunity. *Front Immunol* **11**, 1963 (2020).
33. J. Jeong, Y. Suh, K. Jung, Context Drives Diversification of Monocytes and Neutrophils in Orchestrating the Tumor Microenvironment. *Front Immunol* **10**, 1817 (2019).
34. L. Zhang *et al.*, Tumor-infiltrating lymphocytes genetically engineered with an inducible gene encoding interleukin-12 for the immunotherapy of metastatic melanoma. *Clin Cancer Res* **21**, 2278-2288 (2015).
35. Y. Liu *et al.*, Armored Inducible Expression of IL-12 Enhances Antitumor Activity of Glypican-3-Targeted Chimeric Antigen Receptor-Engineered T Cells in Hepatocellular Carcinoma. *JOURNAL OF IMMUNOLOGY* **203**, 198-207 (2019).
36. B. L. Levine *et al.*, Gene transfer in humans using a conditionally replicating lentiviral vector. *Proc Natl Acad Sci U S A* **103**, 17372-17377 (2006).
37. J. Scholler *et al.*, Decade-Long Safety and Function of Retroviral-Modified Chimeric Antigen Receptor T Cells. *SCIENCE TRANSLATIONAL MEDICINE* **4**, (2012).
38. A. Jolma *et al.*, DNA-binding specificities of human transcription factors. *Cell* **152**, 327-339 (2013).
39. P. Kheradpour, M. Kellis, Systematic discovery and characterization of regulatory motifs in ENCODE TF binding experiments. *Nucleic Acids Res* **42**, 2976-2987 (2014).

Method

TREND library construction

For the generation of the TREND library, we collected PPMs for all human transcription factors from the Bioconductor MotifDb package (v1.46.0) and PWMs from the ENCODE motif compendium(*39*). MotifDb aggregates experimentally determined transcription factor binding profiles derived from SELEX, HT-SELEX, protein-binding microarray (PBM), and ChIP-seq assays across major databases including JASPAR, UniPROBE, hPDI, ScerTF, Stamlab, and cisBP. The ENCODE dataset provided complementary PWMs inferred from large-scale ChIP-seq data across hundreds of transcription factors.

From each matrix, we generated a consensus motif and nine high-probability sequence variants, corresponding to the most likely transcription factor binding sequences derived from nucleotide probabilities within the matrix. Each motif was repeated in tandem with 3 bp spacers between adjacent sites until the total length of the variable region approached 129 bp, ensuring consistent construct size. All variable regions were synthesized as a pooled oligonucleotide library (oligopool) by Agilent Technologies, Inc. (Santa Clara, CA, USA) using array-based DNA synthesis. Each design in the pool contained a variable region comprising tandem transcription factor binding site repeats, flanked by constant elements including universal primer sites and restriction enzyme sites. Each oligonucleotide was then amplified by PCR using primers containing 20 bp random sequences, introducing a unique barcode for quantifying barcode abundance at both the DNA and RNA levels.

The barcode-containing fragments were first digested with AgeI and SbfI and cloned into a lentiviral backbone, generating an intermediate vector. This intermediate construct was then digested again with AscI and BamHI to insert the adenoviral minimal promoter and EGFP reporter gene, yielding the final expression cassette. In this configuration, each enhancer variant regulates EGFP expression, while its associated barcode is positioned at the 3′ end of the EGFP transcript, allowing quantification of barcode abundance at both the DNA and RNA levels. This design enabled quantitative assessment of enhancer activity through barcode-linked expression analysis.

SYNZIP library construction

The Zipper library was designed to systematically evaluate pairwise interactions among 55 synthetic coiled-coil "zipper" domains. All possible 55 × 55 zipper pairs were synthesized as an oligonucleotide pool in the format $zipper_1$-P2A-$zipper_2$, where the self-cleaving P2A peptide separates the two coding sequences. The oligonucleotide pool was synthesized by Agilent Technologies, Inc. (Santa Clara, CA, USA) using array-based DNA synthesis. The synthesized fragments were PCR-amplified and cloned into a GAL4-responsive expression vector containing the GAL4 promoter, such that each fragment was inserted between GAL4BD and VP16AD to generate the fusion construct GAL4BD-$zipper_1$-P2A-$zipper_2$-VP16AD. This configuration allows co-expression of paired zipper domains within the same cell under control of the GAL4 promoter, enabling high-throughput functional screening of zipper-zipper interactions.

Cell culture and cell lines

The human ovarian carcinoma cell line OV8 was originally established at the National Cancer Institute (NCI) and obtained from existing laboratory stocks. BPPNM, KPCA, and PPNM cell lines were gifts from the laboratory of Robert A. Weinberg (Massachusetts Institute of Technology). The ID8 murine ovarian cancer cell line was a gift from the laboratory of Katherine F. Roby (University of Kansas Medical Center). Lenti-X HEK293T (Takara, 632180), CCD-841 CoN cells (American Type Culture Collection, CRL-1790), IOSE (Applied Biological Materials, T1074), and OVCAR-8 were cultured in DMEM (Corning, 10-013-CV) supplemented with 10% fetal bovine serum (FBS; Corning, 35-010-CV), 1% non-essential amino acids (MEM/NEAA; Hyclone, 16777-186), and 1% penicillin–streptomycin (Life Technologies, 15140-122). ID8 cells were cultured in DMEM supplemented with 10% heat-inactivated FBS and 1% penicillin–streptomycin. BPPNM, PPNM, and KPCA cells were cultured in DMEM supplemented with 1% insulin–transferrin–selenium (Thermo Fisher Scientific, 41400045), 2 ng/mL EGF (Life Technologies, PMG8041), 4% heat-inactivated FBS, and 1% penicillin–streptomycin. All cells were maintained at 37 °C in a humidified atmosphere containing 5% CO_2 and were routinely tested negative for mycoplasma contamination.

Primary human T cells

Leukoreduction collars from anonymous healthy platelet donors were obtained through the Brigham and Women's Hospital Crimson Core Laboratory. $CD3^+$ T cells were isolated from the

white blood cell fraction using the RosetteSep Human T Cell Enrichment Kit (STEMCELL Technologies, 15021), followed by density gradient centrifugation with Lymphocyte Separation Medium (Corning, 25-072-CV) and SepMate-50 tubes (STEMCELL Technologies, 85450).

Lentivirus Production and Transduction

Lentiviral particles were generated by reverse transfection of HEK293T cells in a 24-well format using FuGENE-HD (Promega, E2311). All plasmid DNA was normalized to 0.1 µg/µl in sterile water. For each well, a plasmid mixture containing 0.2 µg of lentiviral transfer vector, 0.1 µg psPAX2 (Addgene #12260), and 0.1 µg pVSV-G (Addgene #138479) was prepared. In parallel, 2.4 µl of FuGENE-HD was diluted in 20 µl of Opti-MEM (Thermo Fisher Scientific, 31985070), mixed with the plasmid solution, vortexed briefly, and incubated at room temperature for 15-20 min to allow complex formation.

HEK293T cells were maintained below 80% confluency, and the culture medium was replaced with fresh DMEM 2-4 hours before transfection to promote optimal viral yield. Cells were trypsinized, counted, and resuspended in DMEM to a final concentration of 3.6×10^6 cells/mL. A volume of 100 µl of the cell suspension (3.6×10^5 cells) was added to each transfection tube containing the FuGENE-DNA complexes, mixed gently, and plated into wells pre-filled with 300 µl of fresh DMEM. Eighteen to twenty hours after transfection, the medium was replaced with 500 µl of fresh DMEM. Viral supernatants were harvested 44-48 hours post-transfection, clarified by centrifugation, and filtered through a 0.45 µm syringe filter (Pall Corporation, 4614). Filtered lentivirus was used immediately or stored at 4 °C for up to 3 days or -80 °C for long-term storage.

For transduction, 1.25×10^6 target cells were infected with serial dilutions of filtered viral supernatant in the presence of 8 µg/mL polybrene (Sigma) overnight. Medium was replaced the following day. For comparative experiments, viral titers were normalized using the Lenti-X p24 Rapid Titer Kit (Takara, 631476) before use.

Inducible transcription factor overexpression and reporter assay

A doxycycline-inducible (Tet-On) system was used to regulate TF expression in IOSE cells. IOSE cells were co-infected with three lentiviral vectors: one encoding the reverse tetracycline-controlled transactivator 3 (rtTA3) under the UbC promoter, a second encoding doxycycline-inducible MYC or E2F4 (Tet-On system), and a third carrying the synthetic enhancer-driven EGFP

reporter (MYC_v4 or E2F_v2). Seventy-two hours after infection, cells were treated with increasing concentrations of doxycycline (0, 100, and 1000 ng/mL; Thermo Scientific Chemicals, J60579) for 72 hours to induce graded TF expression. Reporter activity was quantified by flow cytometry (Beckman Coulter, CytoFLEX), and median EGFP fluorescence intensity was analyzed using FlowJo software.

T cell activation and transduction

Cryopreserved primary human T cells were thawed (day 0) and cultured in RPMI 1640 (Corning, 10-040-CV) supplemented with 10% heat-inactivated FBS, 10 mM HEPES (Life Technologies, 15630080), 0.1 mM NEAA, 1 mM sodium pyruvate (Life Technologies, 11360-070), 1% penicillin–streptomycin, 50 μM 2-mercaptoethanol (Sigma-Aldrich, M3148-25ML), and 50 IU/mL recombinant human IL-2 (NCI). T cells were stimulated using the Human CD3/CD28 T Cell Activator (STEMCELL Technologies, 10971) according to the manufacturer's protocol. On day 2, activated T cells were resuspended in lentiviral supernatant and centrifuged at 2,000 × g for 2 h at 32 °C (spinoculation). Viral supernatants were then replaced with fresh culture medium. After transduction, T cells were maintained by diluting 1:2 daily with fresh medium to sustain exponential growth and viability.

For screening and validation of synthetic enhancers, T cells were transduced on day 2 and cultured as described above. On day 10, cells were restimulated with the Human CD3/CD28 T Cell Activator and collected 24 hours later for analysis.

Lentiviral library transduction and sequencing

Pooled lentiviral libraries, including the TREND and Zipper constructs, were packaged and transduced into the respective target cell types using the standard lentiviral production and transduction workflow described above. To ensure reproducibility and minimize sampling bias, we maintained >100-fold representation of each library element throughout the screening pipeline. Five days post-transduction, genomic DNA and total RNA were isolated from pooled cell populations using the AllPrep DNA/RNA Mini Kit (Qiagen, 80204).

DNA library preparation: Barcoded genomic DNA fragments were first amplified by a limited-cycle PCR (3 cycles) using primers that introduced unique molecular identifiers (UMIs), sample indices, and Illumina adapter sequences, enabling simultaneous UMI tagging and adapter

addition while minimizing amplification bias. The resulting products were then amplified in a second PCR (15 cycles) using universal Illumina primers to enrich adapter-ligated fragments and generate sequencing-ready libraries. Amplicons of the expected size (~132 bp) were gel-purified, pooled, and cleaned prior to sequencing.

RNA library preparation: For each sample, 2 µg of total RNA was reverse-transcribed using primers containing a 5′ Illumina adapter, a unique molecular identifier (UMI), and a sample-specific index sequence. Reverse transcription was performed at 42 °C for 60 min, followed by heat inactivation at 85 °C for 5 min. After RNase A treatment, cDNA was amplified by PCR (~15 cycles) using Illumina-compatible universal primers to generate sequencing-ready amplicons (~132 bp). Where indicated, emulsion PCR was tested using Q5 polymerase supplemented with 0.02 mg/mL BSA to reduce amplification bias.

Sequencing libraries were quantified, pooled, and sequenced at the Dana-Farber Cancer Institute Molecular Biology Core Facility on an Illumina NovaSeq platform using 150 bp paired-end reads.

Barcode quantification and enhancer activity analysis

Sequencing data were processed using a custom in-house pipeline implemented on the Harvard Medical School O2 high-performance computing cluster. Read orientation ("flipping") and sample demultiplexing were performed using in-house Python scripts guided by predefined barcode–sample key tables. Demultiplexed reads were collapsed using FASTX-Toolkit (fastx_collapser) to remove duplicate reads, and the resulting files were aligned to the reference library using Bowtie2 with parameters optimized for short, high-similarity sequences. Barcode sequences were then extracted from read pairs using in-house Python and R scripts, and identical barcodes were aggregated to minimize PCR and sequencing biases. Aligned reads were processed with SAMtools to obtain barcode-level count tables for DNA and RNA libraries.

Downstream analysis was performed using an in-house R script. Barcodes with zero DNA or RNA counts were excluded, and constructs represented by fewer than a specified minimal number of independent barcodes were filtered out to ensure reproducibility. For each barcode, the RNA/DNA ratio was calculated as a quantitative measure of enhancer activity. Within each biological replicate, barcode-level ratios were summarized by their median value, and the mean of these replicate medians was used to represent the final enhancer activity score for each construct.

To ensure quantitative robustness, we examined the distribution of DNA barcode for each sample and defined a lower DNA-abundance threshold such that at least 75% of constructs (cancer-specific enhancer project) or 50% of constructs (activation-specific enhancer project) remained transcriptionally active above that cutoff. Barcodes passing this threshold were aggregated by enhancer identity, and constructs meeting coverage criteria were retained for downstream analysis. These activity scores were then used for comparative analysis between tumor and control cell lines or between activated and resting T-cell states. For the cancer-specific enhancer validation experiments, top candidates were selected based on consistent performance across biological replicates. For the activation-specific enhancer validation, top candidates were prioritized from the full library screen in individual donors, with additional preference given to enhancers containing motifs derived from FOS, AP-1, or NFAT families.

Bulk RNA-seq analysis

Total RNA from OV8 and IOSE cells was extracted and submitted to Azenta Life Sciences (GENEWIZ, South Plainfield, NJ, USA) for library preparation and sequencing. RNA quantity was measured using a Qubit 2.0 Fluorometer (Thermo Fisher Scientific), and RNA integrity was assessed with an Agilent TapeStation 4200 (Agilent Technologies). RNA-seq libraries were prepared using the NEBNext Ultra II RNA Library Prep Kit for Illumina (New England Biolabs) with poly(A) selection, following the manufacturer's protocol. Briefly, mRNA was enriched using Oligo(dT) beads, fragmented at 94 °C for 15 min, and reverse-transcribed to generate first- and second-strand cDNA. The resulting cDNA fragments were end-repaired, adenylated at the 3′ ends, ligated to Illumina adapters, and amplified by limited-cycle PCR. Library size and concentration were verified using the Agilent TapeStation and Qubit fluorometer.

Sequencing was performed on an Illumina NovaSeq 6000 platform in a 2 × 150 bp paired-end configuration, targeting approximately 30 million reads per sample. Raw sequencing data were converted to FASTQ format and demultiplexed using bcl2fastq v2.20, allowing one mismatch for index recognition. Adapter trimming and quality filtering were performed with Trimmomatic v0.36. Clean reads were aligned to the human reference genome (ENSEMBL) using STAR v2.5.2b, and gene-level read counts were generated with featureCounts v1.5.2 from the Subread package, considering only uniquely mapped reads within annotated exon regions. Transcript abundance was normalized as TPM for downstream analysis.

Animal experiments

All animal care and experiments were conducted at the Dana-Farber Cancer Institute Animal Research Facility under protocol 19-014, reviewed and approved by the Institutional Animal Care and Use Committee. Mice were housed in ventilated cages (up to five mice per cage) under standard conditions including controlled light/dark cycles, temperature, and humidity.

In vivo antitumor efficacy validation

Three million BPPNM cells engineered to stably express firefly luciferase (BPPNM-Luc) were suspended in a 1:1 mixture of Matrigel (Corning, 47743-710) and phosphate-buffered saline (PBS) and injected intraperitoneally into 6-8-week-old female C57BL/6 mice (Jackson Laboratory, 000664). Tumor progression was monitored by bioluminescence imaging using an IVIS Spectrum imaging system (Xenogen), and images were analyzed with Living Image Software v4.7.4. On day 6 post-implantation, mice were imaged to assess baseline tumor burden; animals showing outlier radiance values were excluded to minimize bias. The remaining mice with comparable radiance levels were then randomly assigned to experimental groups.

For in vivo delivery of the S8IP circuit, lentiviruses encoding each circuit component (module 1, module 2, STE, CD80, IL12, and anti-PD1 antibody) were produced as described above and concentrated tenfold using a Sorvall WX 80+ ultracentrifuge. Concentrated lentiviruses were combined at a volume ratio of module 1 : module 2 : STE : CD80 : IL12 : anti-PD1 = 1 : 1 : 0.5 : 0.5 : 0.5 : 0.5. Lentiviruses for other circuit groups, including SCIP, S8FP, SFIP, S8GP, and SFGP were produced using the same method. Each mouse received an intraperitoneal injection of 400 μL of the viral mixture (~1×10^{10} viral particles/mL), while the higher-dose group received 400 μL at approximately 2×10^{10} viral particles/mL. For control groups, lentiviruses were mixed at identical ratios, substituting the S8IP components with vectors encoding the output reporter rtTA3 or PBS. Viral titers were quantified and normalized before injection using the Lenti-X p24 Rapid Titer Kit (Takara, 631476).

Flow cytometry for immune analysis

BPPNM tumor-bearing mice received an intraperitoneal injection of the S8IP circuit at a dose of 400 μL of viral mixture (~2×10^{10} viral particles/mL) on day 14 after tumor inoculation. Peritoneal

wash was collected 7 days later for analysis. Briefly, mice were euthanized and injected with 5 mL of cold PBS to collect the peritoneal fluid. The collected fluid was centrifuged at 800 x g for 5 min at 4 °C, and the cell pellet was subjected to red blood cell lysis with ACK buffer for 10 min at room temperature. After washing with PBS, cells were resuspended in FACS buffer and passed through 70-μm strainers prior to downstream applications.

For surface staining, cells were first incubated with TruStain FcX™ PLUS (BioLegend, 156603) for 10 min on ice, followed by staining with fluorophore-conjugated antibodies (1:200 dilution, 30 min at 4 °C). After washing with PBS, cells were incubated with Zombie NIR viability dye (BioLegend, 423105; 1:1000 in PBS) for 30 min at 4 °C.

Antibodies used for lymphoid cell analysis include BUV737-CD3 (BD Biosciences, 612821), BV510-CD45 (BioLegend, 103137), BV650-CD4 (BioLegend, 100545), BV711-CD8 (BioLegend, 100747), BV785-CD62L (BioLegend, 104440), Percp Cy5.5-TIM3 (BioLegend, 119717), PE-NK1.1 (BioLegend, 156503), PE/Dazzle 594-CD44 (BioLegend, 103055), PE-Cy7-CD19 (BioLegend, 115519), APC-PD1 (BioLegend, 135210), AF700-CD25 (BioLegend, 102024) and APC-Cy7-CD11b (BioLegend, 101225). APC-Cy7-CD11b was used to exclude $CD11b^+$ cells from lymphoid analysis.

Antibodies used for myeloid cell analysis include BV421-Ly6G (BioLegend, 127627), BV510-CD45 (BioLegend, 103137), BV650-CD11c (BioLegend, 117339), BV785-CD11b (BioLegend, 101243), Percp Cy5.5-Ly6C (BioLegend, 128011), PE-XCR1 (BioLegend, 148204), PE/Cy5-F4/80 (BioLegend, 123111), PE-Cy7-CD172a (BioLegend, 144007), APC-CD206 (BioLegend, 141708), AF700-MHCII (BioLegend, 107621), APC-Cy7-CD3 (BioLegend, 100221) and APC-Cy7-CD19 (BioLegend, 115529). APC-Cy7-CD3 and APC-Cy7-CD19 were used to exclude $CD3^+$ cells and $CD19^+$ cells from myeloid analysis.

For intracellular staining, cells were stimulated in culture at 1×10^6 cells/mL with 2 μl/mL of activation cocktail and GolgiPlug (BD Biosciences, 550583) for 4 h at 37 °C. Cells were washed once and pre-incubated with TruStain FcX™ PLUS for 10 min on ice, followed by surface antibody staining (1:200, 30 min at 4 °C) and Zombie NIR staining (1:1000, 20 min in PBS). After PBS wash, cells were then fixed and permeabilized using the FoxP3/Transcription Factor Staining Buffer Set (eBioscience, 00-5523-00), washed twice with permeabilization buffer, and incubated with intracellular antibodies (1:100 in permeabilization buffer, 1 h at room temperature).

Antibodies used for intracellular cytokines analysis include BUV737-CD3 (BD Biosciences, 612821), BV421-granzyme B (BioLegend, 515409), BV510-CD45 (BioLegend, 103137), BV650-CD4 (BioLegend, 100545), BV711-CD8 (BioLegend, 100747), BV785-IFN-γ (BioLegend, 505838), PE-Perforin (ebioscience, 12-9392-82), PE-Cy7-NK1.1 (BioLegend, 156513), APC-IL-4 (BioLegend, 504105), AF700-Foxp3 (BioLegend, 126421) and APC-Cy7-CD11b (BioLegend, 101225).

Samples were acquired with Cytek Aurora using SpectroFlo v.3.1.0. Collected data were analysed using FlowJo v.10.8.1 Software.

In vivo specificity validation

Three million BPPNM cells were resuspended in a 1:1 mixture of Matrigel (Corning, 47743-710) and PBS and injected intraperitoneally into 6–8-week-old female C57BL/6 mice (Jackson Laboratory). On day 6 post-tumor implantation, mice received 400 μL of lentivirus (~2×10^{10} viral particles/mL) encoding firefly luciferase driven by synthetic enhancers. Luciferase activity was measured on day 18 by in vivo bioluminescence imaging using an IVIS Spectrum imaging system (Xenogen), and analyzed with Living Image Software v4.7.4.

For AND-gate and CMV control groups, lentiviruses were concentrated tenfold using a Sorvall WX 80+ ultracentrifuge and mixed at a volume ratio of module 1 : module 2 : luciferase = 1 : 1 : 2. On day 6, each mouse was administered 400 μL of the viral mixture (~2×10^{10} viral particles/mL) or lentivirus encoding luciferase under the CMV promoter. On day 28, the liver, kidney, spleen, intestine, peritoneal wall, and tumor tissues were harvested for ex vivo bioluminescence imaging.

Statistical analysis

Data were analyzed using GraphPad Prism v10.4.1. The statistical tests applied to each dataset are specified in the corresponding figure legends. Unless otherwise noted, values are presented as mean ± s.e.m. Statistical significance was assessed using unpaired two-tailed Student's t-tests, log-rank (Mantel-Cox) test, one-way analysis of variance (ANOVA) or two-way ANOVA followed by Tukey's multiple comparisons test. Statistical difference was considered significant at *$P < 0.05$, **$P < 0.01$, ***$P < 0.001$. **** $P < 0.0001$.

Materials availability

The TREND library and key plasmids generated in this study will be deposited in Addgene upon publication. Other materials are available from the corresponding author upon reasonable request.

Code and data availability

Processed sequencing data, including post-alignment RNA and DNA barcode count tables for all screens, and summarized screening results will be made available upon publication. The accompanying R scripts for enhancer activity quantification (barcode filtering, normalization, and activity scoring) will be made available alongside the processed data. Raw sequencing data are available from the corresponding author upon reasonable request, in accordance with institutional data-sharing policies.

Acknowledgements

We thank the Molecular Biology Core Facility (MBCF) at Dana-Farber Cancer Institute for technical support and the Animal Research Facility (ARF) for expert animal care. This work was supported by the Cancer Research Institute (CRI) CLIP Award, the Department of Defense Ovarian Cancer Research Program (OC220238/W81XWH-22-OCRP-IIRA), and the Parker Institute for Cancer Immunotherapy.

Author contributions

Y.J., C.-Y.C., and M.-R.W. conceived the study and developed the methodology. Y.J. and M.-R.W. analyzed and interpreted the data and wrote the manuscript. Y.J., C.-Y.C., B.Z., R.W., A.M.S., S.H., Y.-N.L., H.Y., T.S., Y.-C.W. and Z.W. performed experiments and collected data. L.S., Y.W., Y. G., Y.C. and E.B.A. provided technical support and contributed to data interpretation. M.-R.W. supervised the study and coordinated the overall project.

Competing interests

The authors declare that they have submitted patent applications related to the technology described in this study.

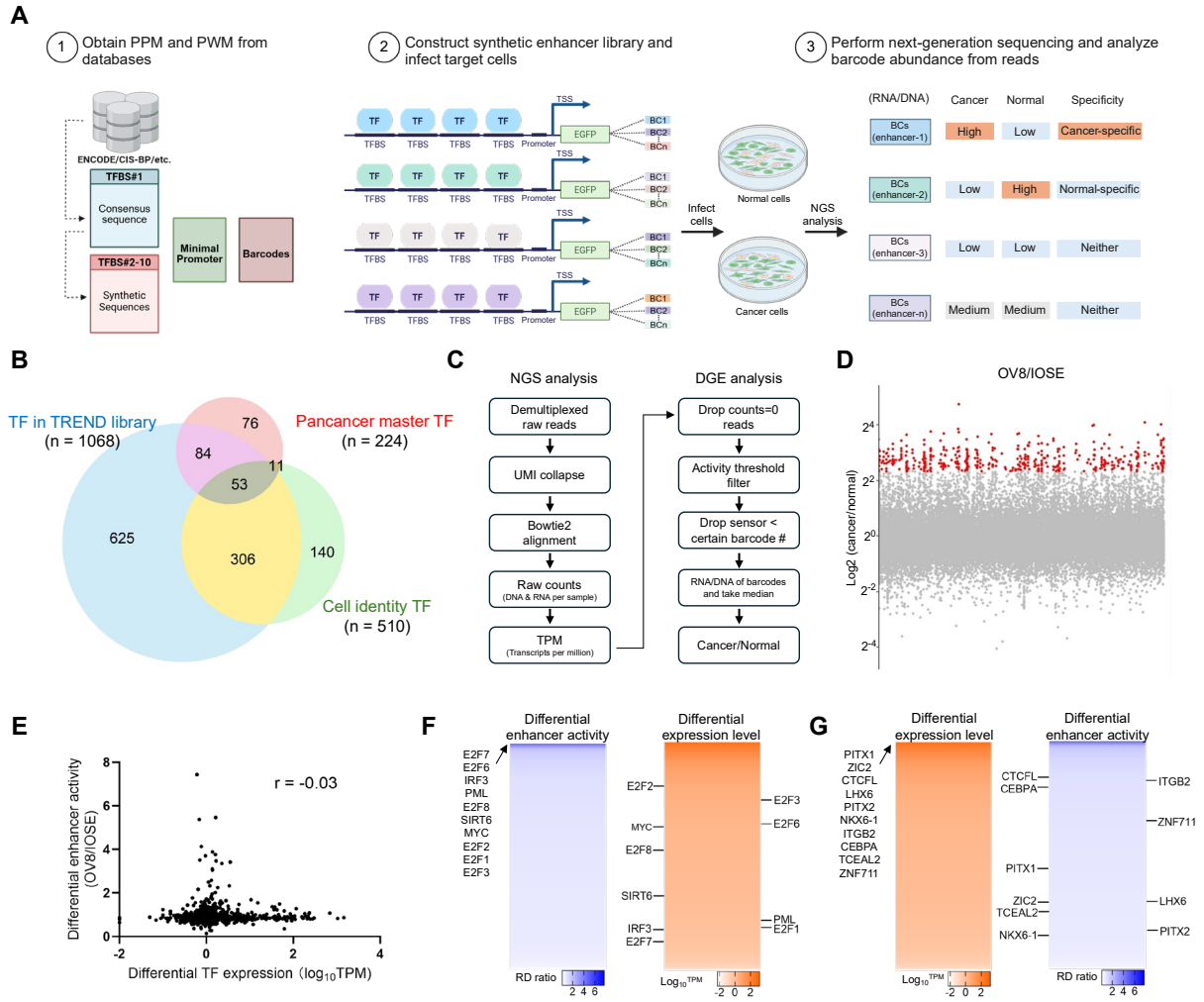

Fig. 1. TREND platform for functional decoding of TF activity. (**A**) Schematic of the TREND workflow for systematic identification of context-specific synthetic enhancers. (1) PPMs and PWMs for 1,068 TFs were obtained from 14 public databases (ENCODE, CIS-BP, etc.) to generate consensus motifs and the nine most probable sequence variants from each matrix. (2) Each motif or variant was concatenated in tandem upstream of an adenoviral minimal promoter and linked to unique DNA barcodes to create a pooled lentiviral library. The library was packaged and delivered into normal and cancer cells. (3) Barcode abundance in RNA and DNA was quantified by targeted NGS, and enhancer activity and specificity were inferred from RNA/DNA ratios across conditions. (**B**) Venn diagram showing overlap of TFs represented in the TREND library with pan-cancer master regulators and cell-identity TF sets. (**C**) Computational pipeline for TREND screening data processing, including demultiplexing, unique UMI collapsing, read alignment, normalization, and activity threshold filtering. (**D**), Differential activity between ovarian cancer (OV8) and normal

ovarian epithelial (IOSE) cells, highlighting cancer-selective synthetic enhancers (red) with high cancer-to-normal ratios. (**E**) Scatterplot comparing differential TF mRNA expression (OV8 versus IOSE) with the corresponding differential activity (OV8 versus IOSE) of the synthetic enhancers responsive to each TF, measured by TREND. Each point represents a specific TF. (**F** and **G**) Heatmaps comparing differential enhancer activity (OV8/IOSE activity ratio) of TREND-identified synthetic enhancers with the corresponding TF differential expression (OV8/IOSE, RNA-seq). TFs associated with top-performing cancer-specific enhancers are dispersed throughout the TF differential-expression landscape rather than concentrated among highly differentially expressed TFs (F), and conversely, TFs with high transcript differences are distributed across a wide range of enhancer specificity without a consistent trend (G).

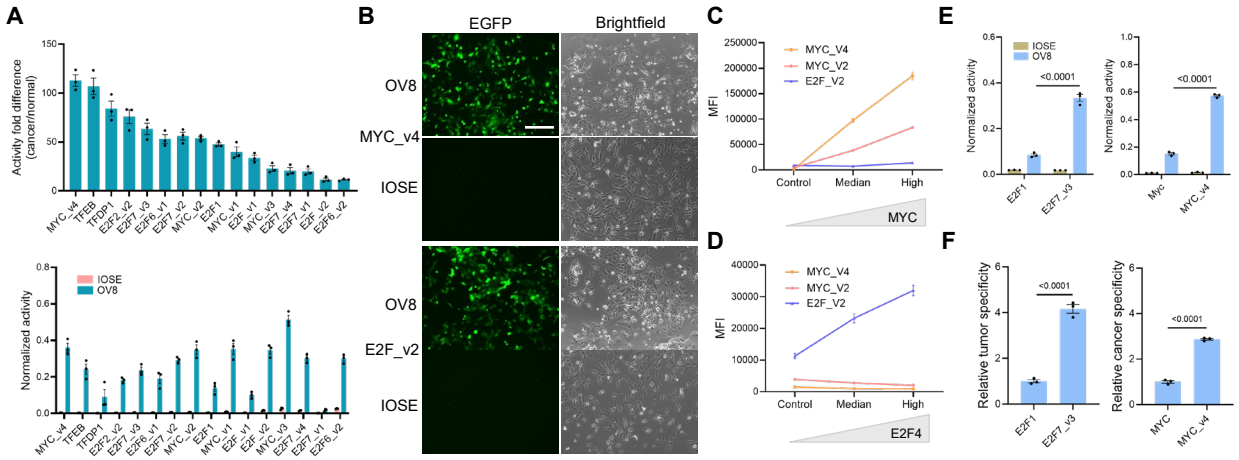

Fig. 2. Cancer-selective synthetic enhancers report cognate TF activity. (**A**) Quantitative reporter assays of individually cloned synthetic enhancers in human ovarian cancer (OV8) and normal ovarian epithelial (IOSE) cells measured by flow cytometry. Enhancer activity was normalized to the constitutive ubiquitin C (UbC) promoter control, and the activity fold difference was calculated as the ratio of normalized activity in OV8 cells relative to IOSE cells. v1, v2, v3, v4, etc. represent distinct motif variants derived from the same TF. (**B**) Representative fluorescence microscopy images of OV8 and IOSE cells transduced with MYC_v4 or E2F_v2 synthetic enhancers driving EGFP expression. Scale bar, 200 µm. (**C** and **D**) Reporter assays showing doxycycline dose-dependent activation of MYC_v4 and MYC_v2 (C) or E2F_v2 (D) enhancers following induction of their cognate TFs (MYC or E2F4) in IOSE cells. Data show median fluorescence intensity (MFI) of EGFP (n = 3) measured by flow cytometry. (**E** and **F**) Comparison of TREND-derived synthetic enhancers with previously reported designs in OV8 cells. E2F7_v3 and MYC_v4 were identified by TREND, whereas E2F1 and MYC represent previously reported enhancers. (E) Reporter activity driven by each enhancer. (F) Relative cancer specificity calculated as the ratio of enhancer activity in OV8 versus IOSE cells, with values normalized to the previously reported E2F1 and Myc enhancers. Data are mean ± s.e.m. from three independent experiments. Statistical significance was determined by unpaired two-tailed Student's t-tests.

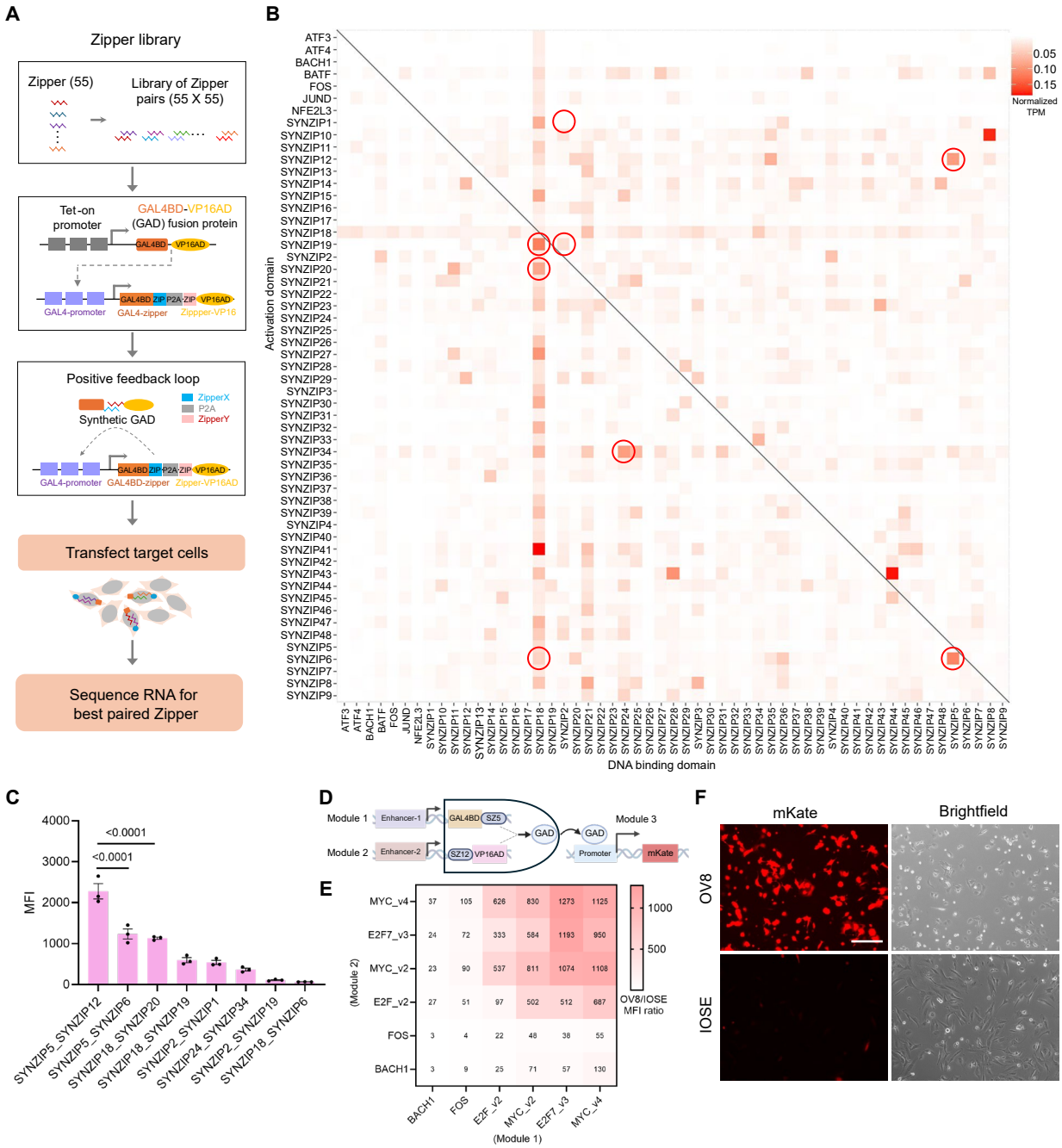

Fig. 3. Enhancer-driven AND-gate circuits integrate multiple TF activities via protein–protein interactions. (**A**) Overview of the coiled-coil interaction screen used to identify optimal zipper pairs for circuit design. Each candidate coiled-coil domain was fused to either the GAL4BD-zipper or the zipper-VP16AD and expressed in HEK293T cells. Productive interactions between complementary zippers reconstitute a functional GAD, which drives reporter expression from a GAL4-responsive promoter. Transcript quantification by RNA sequencing was used to

identify the most efficient interacting pairs. (**B**) Heatmap of pairwise interactions among 55 coiled-coil domain combinations, highlighting high-activity pairs (circled). (**C**) Flow-cytometry analysis of reporter activity for selected zipper pairs in HEK293T cells. (**D**) Schematic of the enhancer-driven AND-gate circuit, in which two distinct TREND enhancers independently drive GAL4BD-zipper and zipper-VP16AD expression. Productive coiled-coil pairing between the two proteins reconstitutes an active GAD complex, enforcing AND logic at the transcriptional level. (**E**) Cancer-to-normal activity ratios of AND-gate constructs assembled from synthetic enhancers MYC_v4, E2F7_v3, MYC_v2, E2F_v2, FOS, and BACH1, showing varying degrees of cancer selectivity. Heatmap values represent the mean from three independent experiments. (**F**) Representative fluorescence-microscopy images of mKate reporter in OV8 and IOSE cells transduced with the AND-gate construct. Scale bar, 200 μm. Data are mean ± s.e.m. from three independent experiments. Statistical significance was determined by one-way ANOVA with Tukey's multiple-comparisons test.

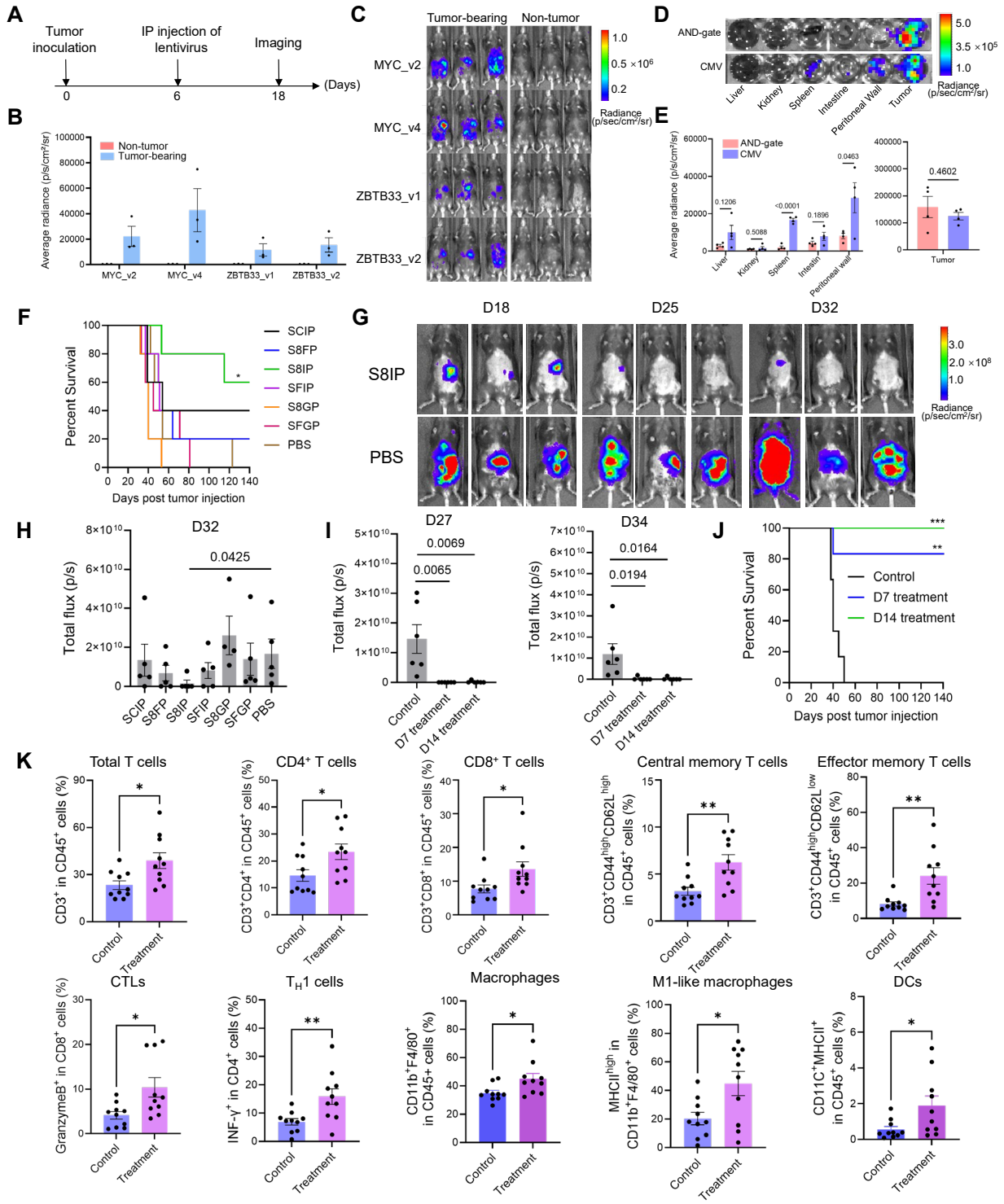

Fig. 4. Tumor-restricted AND-gate circuits reprogram the tumor microenvironment and elicit durable therapeutic responses in murine ovarian cancer. (**A**) Experimental design for testing tumor specificity of individual TREND-derived synthetic enhancers in BPPNM tumor-bearing mice. (**B**) Quantification of bioluminescence signals from tumor-bearing and tumor-free

mice (n = 3 mice per group). (**C**) Representative bioluminescence images of mice bearing BPPNM tumors or tumor-free controls following transduction with luciferase driven by single synthetic enhancers. (**D**) Ex vivo bioluminescence imaging of organs from mice transduced with enhancer-driven AND-gate circuits or CMV promoter-driven luciferase. (**E**) Quantification of luciferase activity across major normal organs following delivery of AND-gate circuits or CMV enhancer constructs (n = 4 mice per group). (**F**) Survival curves of BPPNM tumor-bearing mice treated with AND-gate circuits encoding different combinations of immune effectors (n = 5 per group). (**G**) Representative bioluminescence images of tumor burden in treated mice. (**H**) Quantification of tumor growth on day 32 based on bioluminescence imaging (n = 5 per group). (**I**) Quantification of tumor growth in BPPNM tumor-bearing mice treated with a two-fold higher dose (relative to panels (F and H)) of the S8IP circuit, administered on day 7 or day 14 after tumor inoculation (n = 6 per group). (**J**) Survival curves of mice treated with the S8IP circuit on day 7 or 14, showing prolonged survival with both early and delayed dosing (n = 6 per group). (**K**) Flow-cytometry analysis of peritoneal immune cells following S8IP circuit treatment. BPPNM tumor-bearing mice were treated with the S8IP circuit at the dosage used in panels (I and J), administered on day 14 after tumor inoculation. Peritoneal wash was collected 7 days later for analysis. n = 10 per group. Statistical significance was determined by unpaired two-tailed t-tests, one-way ANOVA with Tukey's multiple-comparisons test or log-rank (Mantel-Cox) test. *$P < 0.05$, **$P < 0.01$, ***$P < 0.001$ and ****$P < 0.0001$.

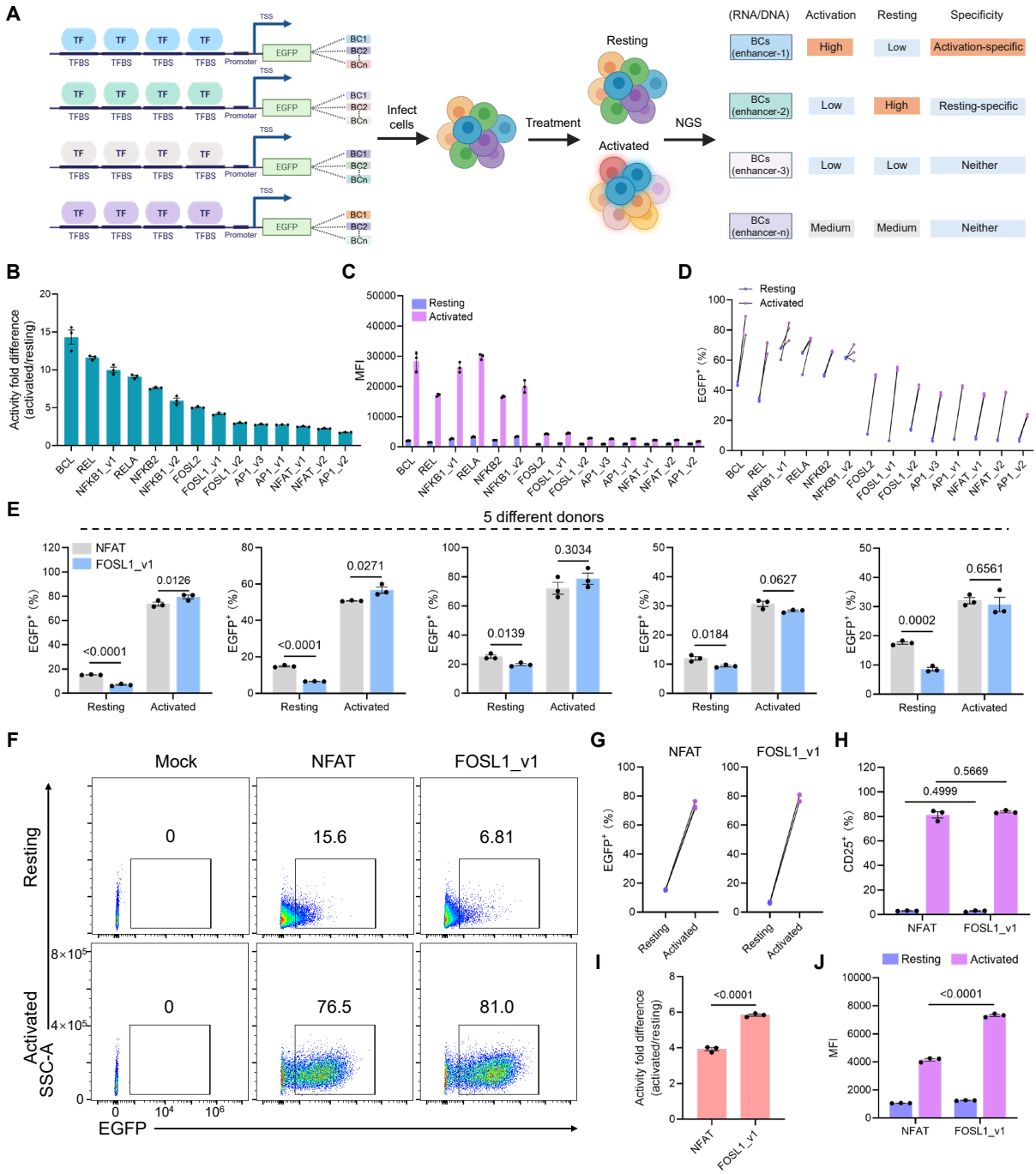

Fig. 5. Identification of activation-responsive synthetic enhancers in T cells. (**A**) Schematic of the pooled screening workflow in human primary T cells. Cells were transduced with the TREND library, stimulated with anti-CD3/CD28 antibody, and enhancer activity was quantified by sequencing barcode-linked transcripts. (**B**) Fold difference in reporter activity (activated relative to resting condition) for all tested enhancers, identifying candidates responsive to T cell activation. (**C**) MFI of EGFP expression driven by individual enhancers in activated versus resting

T cells. (**D**) Percentage of $EGFP^+$ T cells under activated and resting conditions, showing activation-induced enhancer responsiveness. (**E**) Comparison of $EGFP^+$ cell percentages for the canonical NFAT-motif-based enhancer and the TREND-derived FOSL1_v1 enhancer under activated and resting conditions. (**F**) Representative flow cytometry analysis showing EGFP expression driven by NFAT and FOSL1_v1 enhancers in resting and activated T cells. (**G**) Quantification of $EGFP^+$ cell percentages from panel (F). (**H**) Proportion of $CD25^+$ T cells transduced with NFAT or FOSL1_v1 enhancer under resting and activated conditions. (**I**) Fold difference in reporter activity (activated relative to resting condition) for NFAT and FOSL1_v1 enhancers. (**J**) MFI of EGFP expression for NFAT and FOSL1_v1 enhancers in activated and resting T cells. Data are mean ± s.e.m. from three independent experiments. Statistical significance was determined by unpaired two-tailed t-tests.

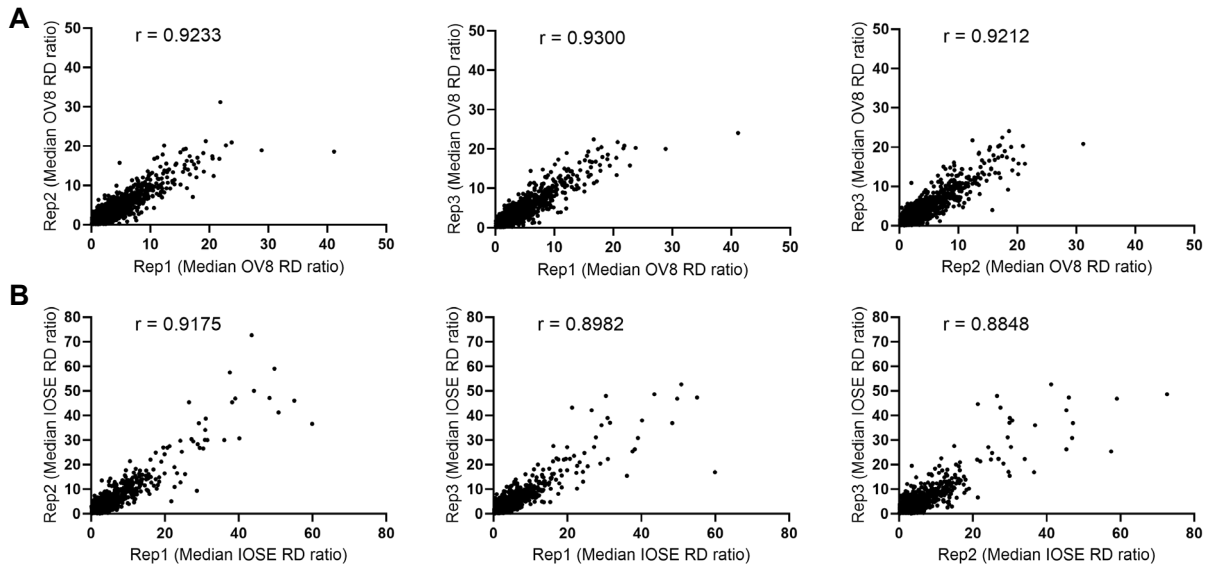

Fig. S1. TREND screening shows high reproducibility across biological replicates. (**A** and **B**) Correlation of synthetic enhancer activity profiles between independent biological screening replicates in OV8 (A) and IOSE (B) cells. Each point represents a synthetic enhancer, with RNA output normalized to DNA input (RNA/DNA ratio, referred to as RD ratio). Pearson correlation coefficients indicate high reproducibility between TREND screening replicates.

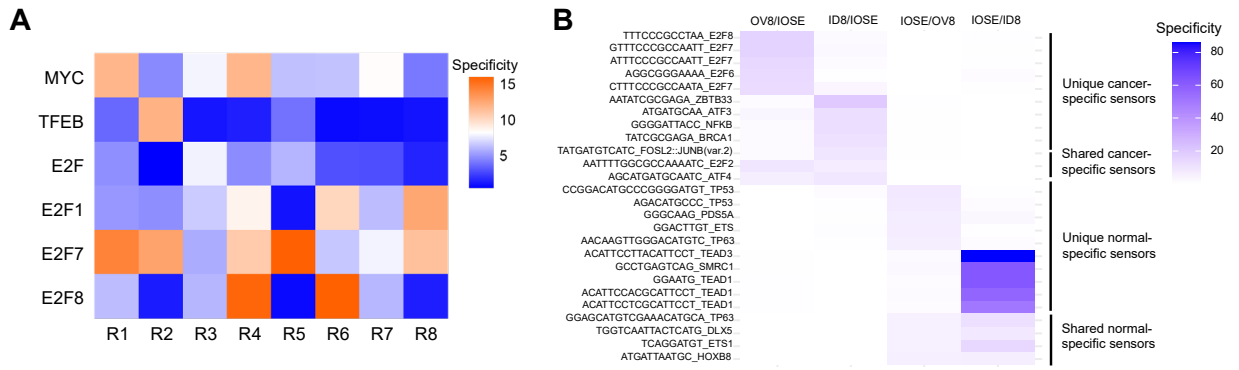

Fig. S2. Relationship between motif variant rank and synthetic enhancer activity. (**A**) Heatmap showing the relationship between motif variant rank within the PPM and enhancer specificity across TFs. Highly cancer-specific enhancers can arise from any motif rank, whether consensus or lower-ranked variants, rather than clustering at a particular rank. (**B**) Representative classes of enhancers, including those selective for human cancer cells (high OV8/IOSE), mouse cancer cells (high ID8/IOSE), and shared cancer-selective elements active in both human and mouse cancer cells (high OV8/IOSE and ID8/IOSE), as well as enhancers preferentially active in normal human epithelial cells (high IOSE/OV8, high IOSE/ID8, or both). The heatmap values denote the specificity, defined as the activity ratio between cell types.

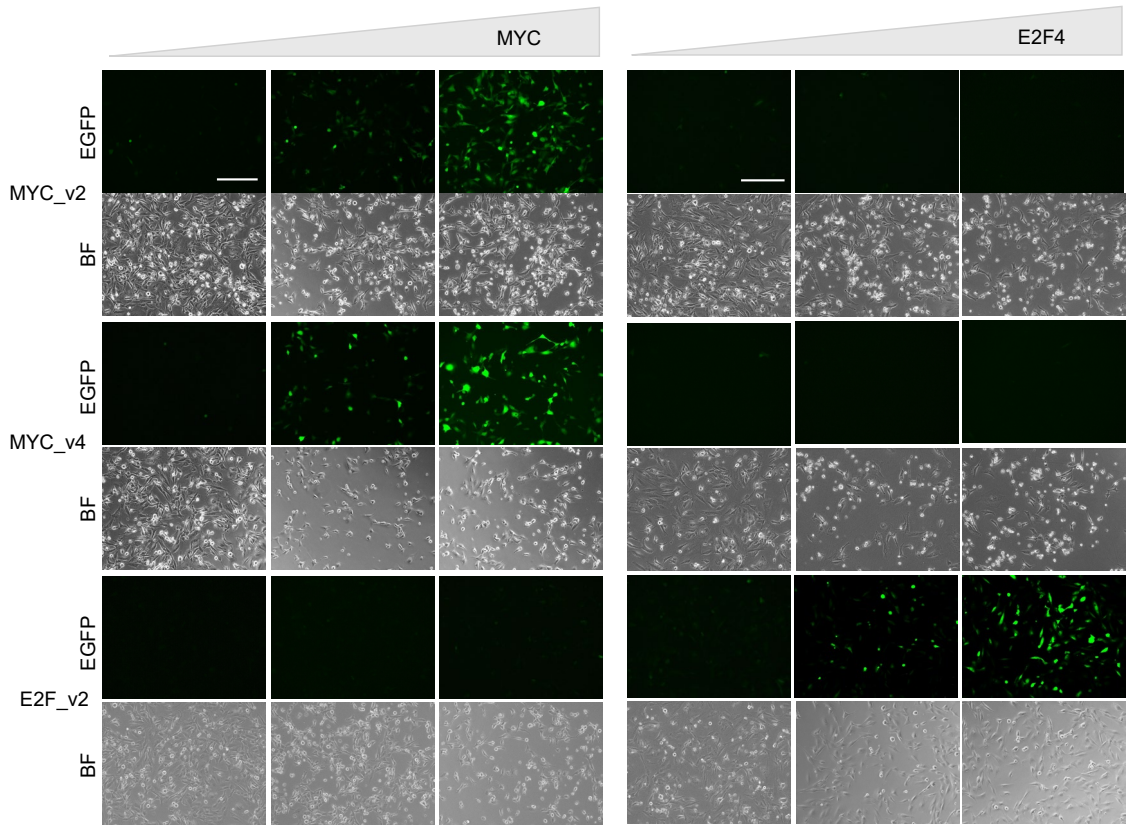

Fig. S3. Dose-response of TREND-derived synthetic enhancers to TF abundance. Fluorescence microscopy images of IOSE cells co-transduced with MYC_v4 or E2F_v2 synthetic enhancers and a Tet-ON-inducible TF expression cassette for overexpressing MYC or E2F4. Images show graded reporter activation in response to TF abundance. Scale bar, 300 μm. Data are representative of three independent experiments.

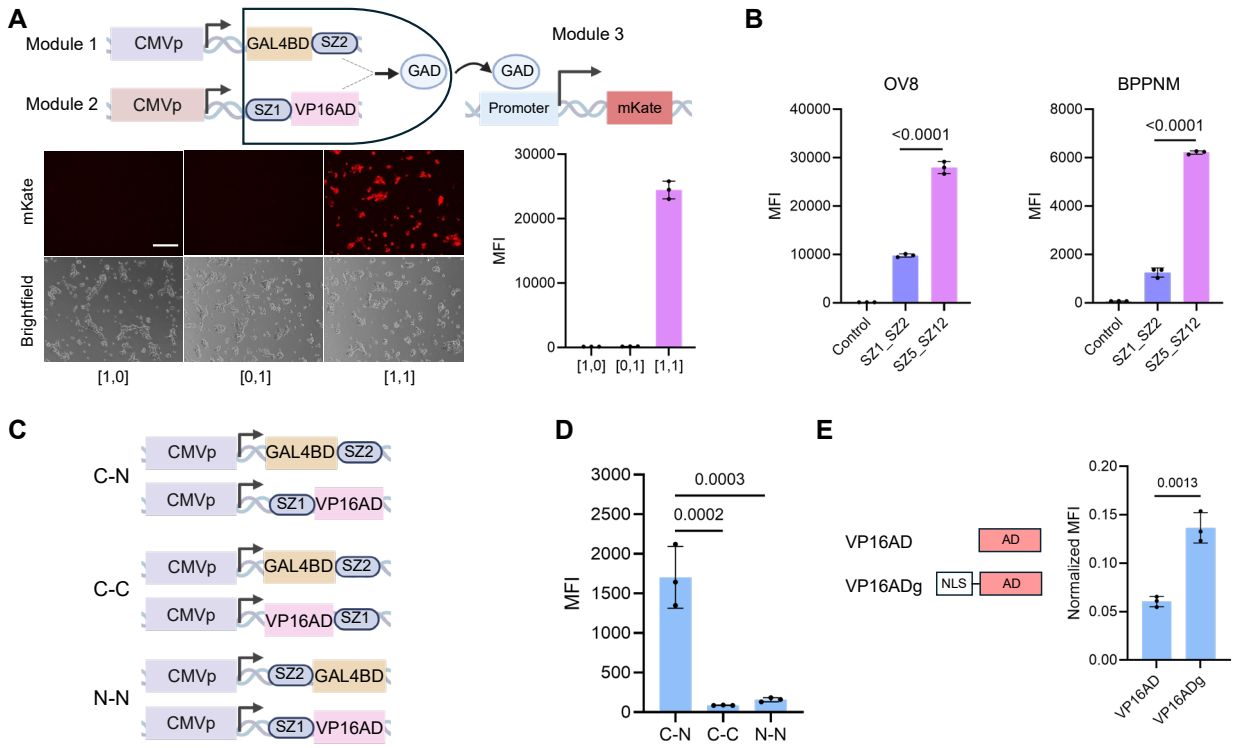

Fig. S4. Orientation-dependent effects and nuclear localization enhance SYNZIP-based AND-gate performance. (**A**) Reporter assays of partial AND-gate configurations, showing that incomplete circuits containing only one enhancer input ([1,0] or [0,1]) fail to activate transcription. Scale bar, 200 µm. (**B**) Validation of SYNZIP-based AND-gate activity in human (OV8) and mouse (BPPNM) ovarian cancer cells. (**C**) Schematic illustrating different orientations of SYNZIP fusion to GAL4BD and VP16AD domains. (**D**) Quantification of reporter activity across different SYNZIP fusion orientations. (**E**) Effect of a nuclear localization signal (NLS) to VP16AD on downstream reporter expression. Data represent mean ± s.e.m. from three independent experiments. Statistical significance was determined by unpaired two-tailed t-tests or one-way ANOVA with Tukey's multiple-comparisons test.

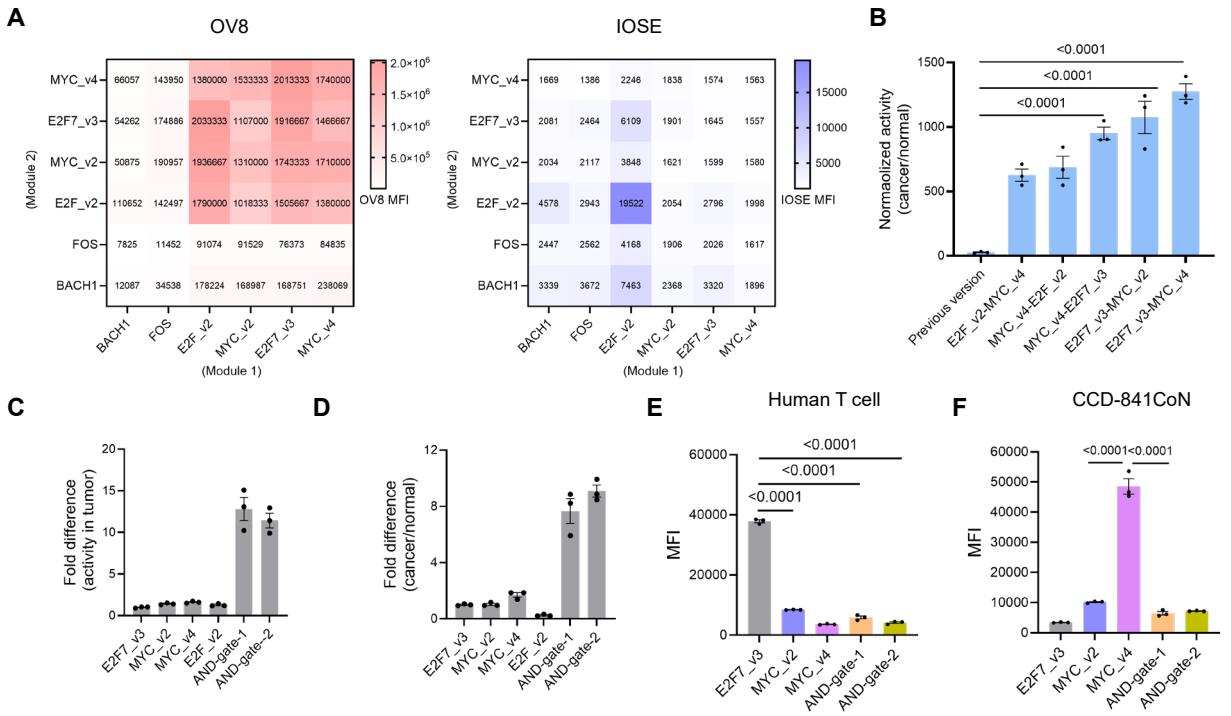

Fig. S5. Functional evaluation of AND-gate circuits constructed from TREND-derived synthetic enhancers. (**A**) Reporter assays comparing the activity of AND-gate constructs in OV8 and IOSE cells. Each construct was assembled from validated TREND-derived enhancers (MYC_v4, E2F7_v3, MYC_v2, E2F_v2, FOS, and BACH1), evaluated in different pairwise combinations. Heatmap values represent the mean from three independent experiments. (**B**) Comparison of cancer specificity between the top five AND-gate designs and a previously published AND-gate configuration. Fold change represents the ratio of MFI in OV8 relative to IOSE. (**C**) Quantification of transcriptional output from AND-gate constructs relative to single synthetic enhancers. AND-gate architecture amplifies output strength, with activity normalized to the E2F7_v3 single-enhancer group. (**D**) Comparison of cancer-to-normal discrimination ratios between AND-gate and single-enhancer constructs. (**E** and **F**) Reporter activity of single synthetic enhancers and AND-gate constructs in human T cells and normal colon epithelial CCD-841 CoN cells. AND-gate-1 contains E2F7_v3 and MYC_v2 synthetic enhancers, and AND-gate-2 contains E2F7_v3 and MYC_v4 synthetic enhancers (E and F). Data are mean ± s.e.m. from three independent experiments. Statistical significance was determined by one-way ANOVA with Tukey's multiple-comparisons test.

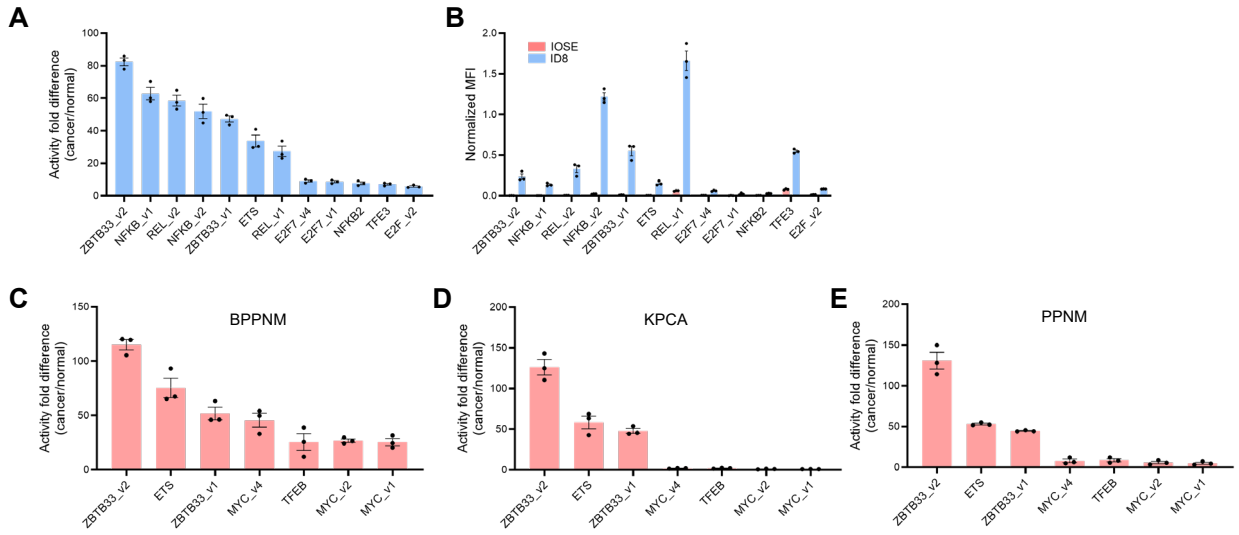

Fig. S6. Screening and validation of murine cancer-specific synthetic enhancers. (**A**) Tumor specificity of TREND-derived synthetic enhancers in ID8 mouse ovarian cancer cells, quantified as the fold difference in activity relative to normal human ovarian epithelial cells (ID8/IOSE). (**B**) Normalized enhancer activity in ID8 and IOSE cells corresponding to the data in panel a, illustrating relative enhancer activity across cancer and normal contexts. MFI values were normalized to the UbC promoter control. (**C** to **E**) Validation of synthetic enhancer activity across additional mouse ovarian cancer cell lines, including BPPNM (C), KPCA (D), and PPNM (E). Activity fold difference represents the ratio of MFI in BPPNM/IOSE, KPCA/IOSE, and PPNM/IOSE, respectively. Data are mean ± s.e.m. from three independent experiments.

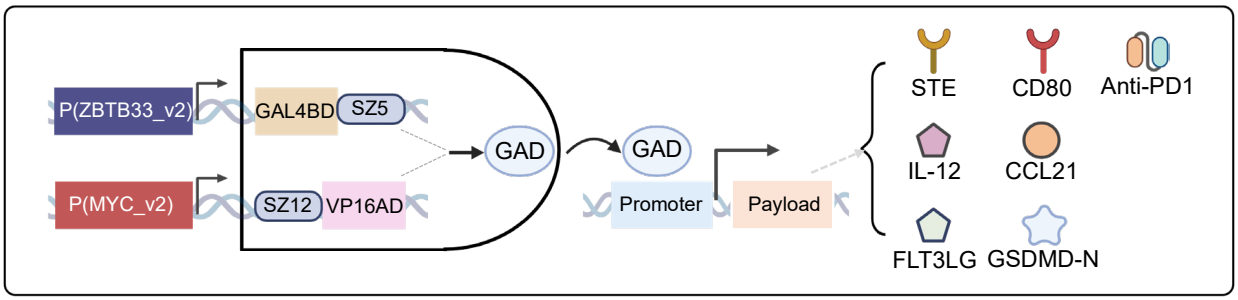

Fig. S7. Schematic of the cancer-restricted AND-gate design. Two TREND-derived synthetic enhancers independently drive GAL4BD and VP16AD expression; coiled-coil pairing reconstitutes a synthetic transcription factor (GAD) that activates downstream therapeutic payloads, enabling cancer-selective expression of multiple immune effectors.

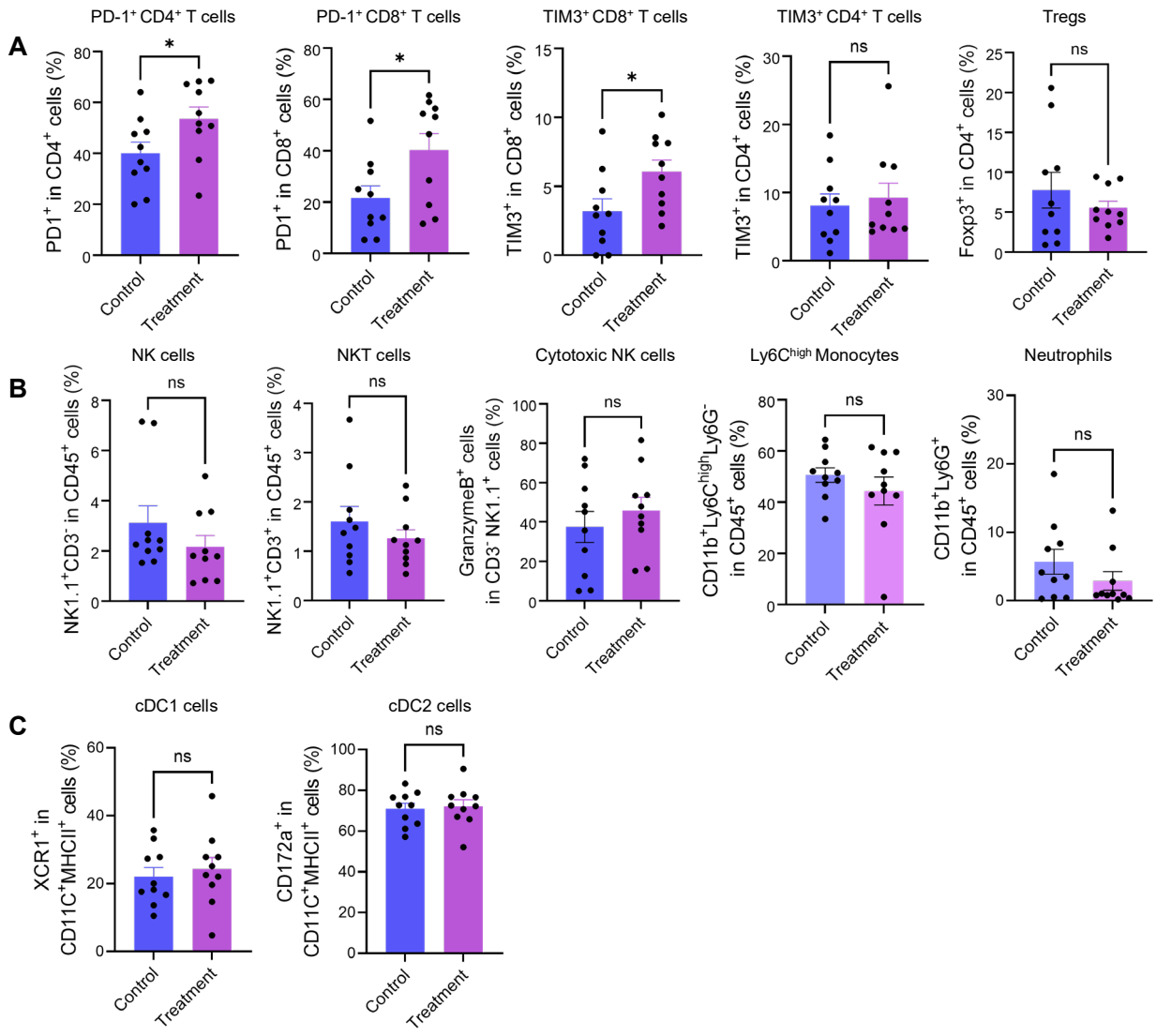

Fig. S8. Characterization of tumor microenvironment (TME) immune composition following treatment with the AND-gate circuit expressing the S8IP output combination. (**A**) Flow-cytometric analysis of T-cell subsets in the peritoneal TME, showing proportion of PD-1^{+} CD4^{+} T cells, PD-1^{+} CD8^{+} T cells, TIM-3^{+} CD8^{+} T cells, TIM-3^{+} CD4^{+} T cells, and Tregs. (**B**) Proportion of innate immune populations including NK cells, NKT cells, cytotoxic NK cells, Ly6C^{high} monocytes and neutrophils. (**C**) Proportion of cDC1 and cDC2 in the TME. Data represent mean ± s.e.m. from 10 mice per group. Statistical significance was determined by unpaired two-tailed t-tests.

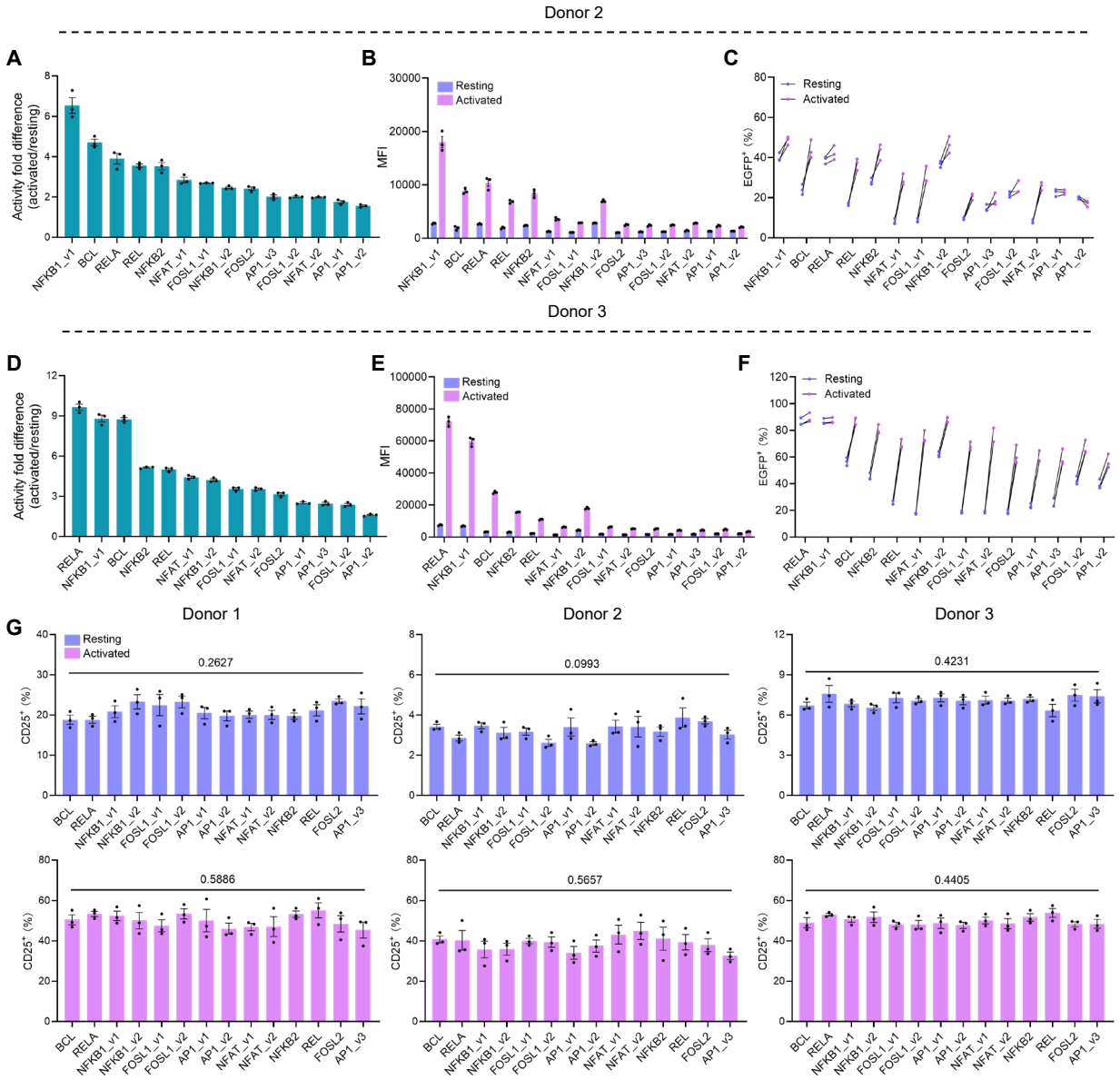

Fig. S9. Validation of activation-responsive synthetic enhancers in primary human T cells. (**A** and **D**) Fold change in reporter activity (activated/resting) for all tested enhancers, identifying candidates responsive to T-cell activation. (**B** and **E**) Raw MFI of EGFP expression driven by individual enhancers under activated and resting conditions. (**C** and **F**) Percentage of EGFP$^+$ T cells under activated versus resting conditions. (**G**) Proportion of CD25$^+$ T cells transduced with individual enhancers under resting and activated conditions, summarized across three independent donors. Data represent mean ± s.e.m. from three independent experiments. Statistical significance was determined by unpaired two-tailed t-tests or one-way ANOVA.

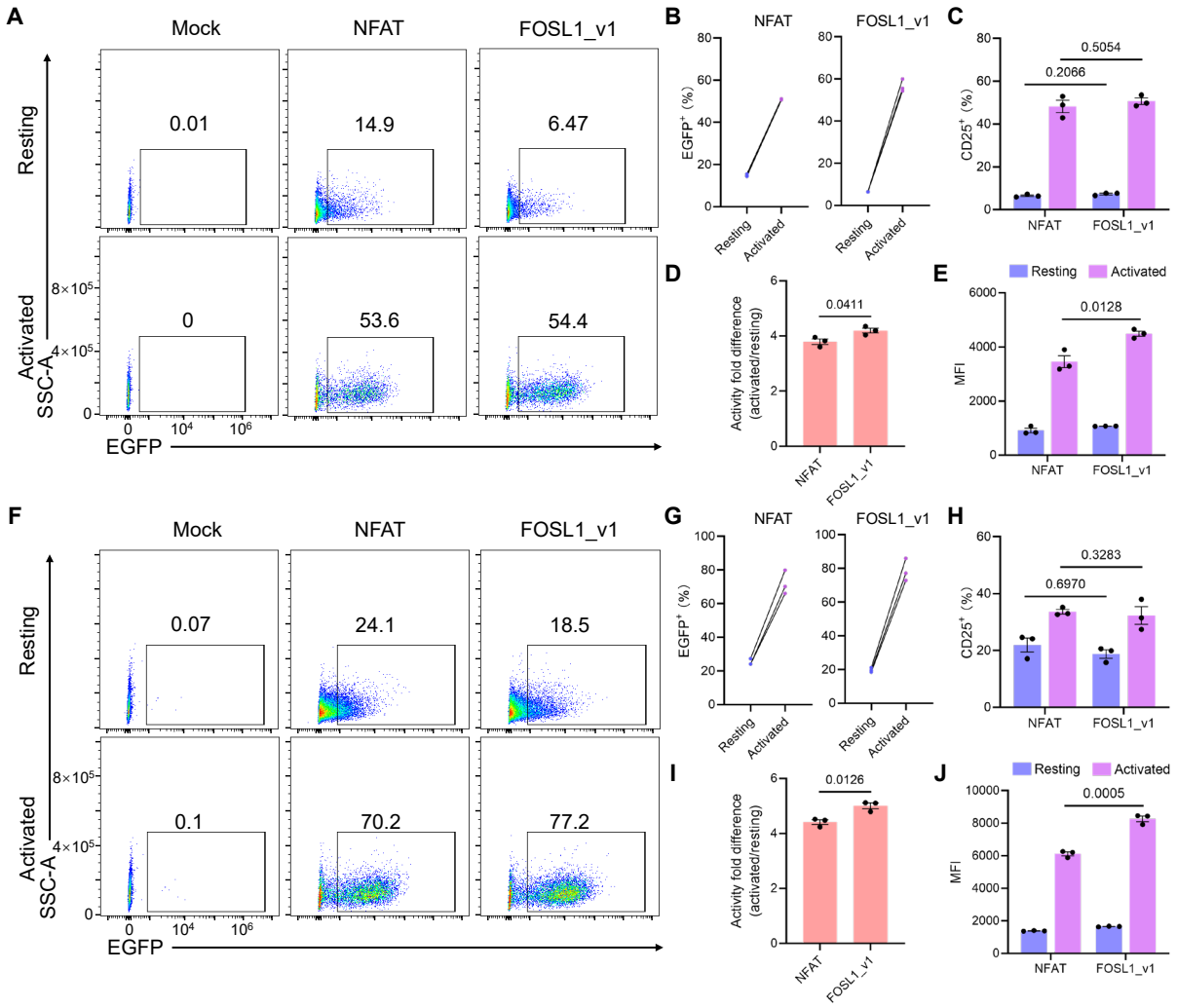

Fig. S10. Comparison of NFAT and FOSL1-motif-based synthetic enhancer in T cells. (**A** and **F**) Representative flow cytometry plots showing EGFP expression driven by NFAT and FOSL1_v1 enhancers in resting and activated T cells. (**B** and **G**) Quantification of EGFP$^+$ cell percentages from panels (A) and (F). (**C** and **H**) Proportion of CD25$^+$ T cells transduced with NFAT or FOSL1_v1 enhancers under resting and activated conditions. (**D** and **I**) Fold change in reporter activity (activated relative to resting) for NFAT and FOSL1_v1 enhancers. (**E** and **J**) MFI of EGFP expression for NFAT and FOSL1_v1 enhancers in activated and resting T cells. Panels (A to E) and (F to J) show data from two different donors. Data are mean ± s.e.m. from three independent experiments. Statistical significance was determined by unpaired two-tailed t-tests.